Supporting Information

Multiplex Profiling of Biomarkers and Drug Uptake in Single Cells Using Microfluidic Flow Cytometry and Mass Spectrometry

Xuan Zhang[1,2,4], Xing Wei[1], Cheng-Xin Wu[1], Xue Men[1], Jiao Wang[1], Jun-Jie Bai[1], Xiao-Yan Sun[1], Yu Wang[1], Ting Yang[1], Chwee Teck Lim[2,3,*], Ming-Li Chen[1,*], Jian-Hua Wang[1,*]

1. *Research Center for Analytical Sciences, Department of Chemistry, College of Sciences, Northeastern University, Box332, Shenyang 110819, China.*
2. *Institute for Health Innovation and Technology, National University of Singapore, Singapore 117599, Singapore.*
3. *Department of Biomedical Engineering, National University of Singapore, Singapore 117576, Singapore*
4. *Academy of Medical Science, Shanxi Medical University, Taiyuan 030001, China.*

Corresponding Authors

*E-mail address: ctlim@nus.edu.sg (C. T. Lim); chenml@mail.neu.edu.cn (M.-L. Chen); jianhuajrz@mail.neu.edu.cn (J.-H. Wang).

Supporting Information

Experimental

Materials and chemicals

RTV 615 poly (dimethylsiloxane) (PDMS) pre-polymer and curing agent were purchased from Momentive Performance Materials (Waterford, NY, USA). Surface-oxidized silicon wafers were obtained from Shanghai Xiangjing Electronic Technology, Ltd. (Shanghai, China). SU8-2050 photoresist was provided by MicroChem (Newton, MA, USA). Nitric acid and hydrogen peroxide were the products of Sinopharm Chemical Reagent Co., Ltd (Shanghai, China). Tween 20 was received from Aladdin Reagent Co., Ltd (Shanghai, China). Platinum standard was obtained from National Research Center for Certified Reference Materials (Beijing, China). Standard gold nanoparticles solution (with the particle size of 60.8 ± 7.5 nm) was purchased from BBI Solutions (UK). Dulbecco's modified Eagle's medium (DMEM), fetal bovine serum (FBS), trypsin and phosphate buffer solution (PBS) were the products of Gibco Invitrogen Corporation (CA, USA). The analytical reagent-grade solvents and other chemicals were received from the local commercial suppliers, unless otherwise specified. All solutions were prepared using ultra-purified water supplied by a Milli-Q system (Millipore®).

Apparatus and Imaging analysis

Two syringe pumps (Pump 11 Elite, Harvard, USA) and a triple-quadrupole inductively coupled plasma mass spectrometer (Agilent 8900, Agilent Technologies,

CA, USA) were used for the study. ICP-MS was used to monitor ^{197}Au or ^{195}Pt isotopes in isolation. Monitoring of ^{197}Au isotopes was used to assess the single-cell sample transfer efficiency of this system, while monitoring of ^{195}Pt isotopes was used to analyze the uptake of platinum-based drugs in different single cells. The generation of aerosol used an Enya Mist nebulizer and horizontal micro spray chamber whose detailed parameters are shown in Figure S24D. On general analysis, the dwell time was set at 0.1 ms. The spectrometer was tuned daily with an aqueous multi-element standard solution (containing 10 μg/L Li, Y, Co, Ce, Tl) for controlling consistent sensitivity and minimum levels of doubly charged ions and oxide species of ^{140}Ce. ICP-MS was used to monitor ^{195}Pt isotopes to assess the uptake of oxaliplatin in a single cell. At the same time, a laser-induced fluorescence detector (LIF) built by the group was used to monitor the fluorescence intensity of a BioNPs probe labelled on the cell surface in order to assess the PTK7 expression level in the same single cell. An inverted microscope (Olympus, BX53M) with a charge coupled device camera (Olympus, DP74), a mercury lamp (Olympus, U-RFLT50), and a high-speed camera (Olympus i-speed TR, Japan) were used for cell monitoring and fluorescence observation. The imaging and data analyses were carried out using Image-Pro1 Plus 6.0 (Media Cyternetics, Silver Spring, MD), Image J v1.8.0 (National Institutes of Health), and origin 9.5 (origin Inc.).[1-2]

Preparation and characterization of BioNPs conjugates

Standard AuNPs (60.8 nm) were prepared with a concentration of ~2.5 nM.[3] The

Sgc8 aptamer was thiol-modified at 5' terminal and 6-FAM was labeled at 3' terminal. Both were synthesized by Sangon Biotech (Shanghai, China). A 6-FAM labeled thiol-modified Sgc8 was used to modify AuNPs for quantifying the number of aptamer strands attached to each AuNP. The Sgc8 sequence was 5' thiol-C6-TTTTTTTTTTATCTAACTGCTGCGCCGCCGGGAAAATACTGTACGG TTAGA-6-FAM. Thiol-modified sequences were applied as received without DTT or TCEP treatment. Thiol-modified DNA (100 μM, 7.5 μL) was mixed with citrate-AuNPs (60.8 nm, ~1.0 nM, 1000 μL), and the mixture was divided into 10 Eppendorf tubes with 100 μL per tube. All the tubes were placed in a freezer (–20 ℃) for 2 h, and then thawed at room temperature. The diameters of Sgc8-AuNPs conjugates were measured by transmission electron microscopy (TEM).

To quantify the number of aptamer strands attached to each AuNP, we used the excess GSH to displace Sgc8 from the AuNPs. The concentration of the displaced Sgc8 aptamer in the supernatant was then obtained as 2958.3 ± 81.0 nM by comparing its fluorescence intensity against the calibration curve (n=3). Thus, the concentration of Apt Sgc8 bound to the AuNPs was 634.6 nM, and the final concentration ratio of DNA to AuNPs was 2958.3 nM : 1.0 nM. Thus, ~ 2958 Sgc8 aptamers were loaded on each AuNP (60.8 nm).

Binding affinities analysis

To determine the binding affinities of Sgc8-AuNP conjugates and Sgc8 against cells, adhesive MCF-7 cells (about 10^5 cells) were incubated with a series of

concentrations of the above mentioned aptamer AuNP/aptamer conjugates in 200 μL buffer (PBS with 5 mM $MgCl_2$, pH = 7.4) on ice for 5, 10, 15, 20, 25, 30 min respectively for optimizing of treatment time of BioNPs nanoprobes conjugating on MCF-7 cells. Cells were washed twice with cold buffer. Cells were then analyzed by a microplate reader (Synergy H1, BioTek, USA). The experimental conditions were the same as those described above. The dissociation constants values (K_d) were obtained by fitting the dependence of fluorescence intensity (Y) on the concentration of ligands (X) to the equation $Y=B_{max}X/(K_d+X)$ by SigmaPlot software. B_{max} is the maximum binding amount.

Numerical simulations

To evaluate the fluid flow and vortex distribution in the microfluidic system, computational fluid dynamics (CFD) simulation was performed using Comsol Multiphysics 5.4 (Comsol) on an eight-core, 64-bit computer (Asus) with 64 GB of RAM. The simulation environment was verified for steady-state incompressible flows in the section of "*Dean*-like secondary flow acceleration". Different flow rates were specified at the inlet, and the outlet was set to a fixed-pressure boundary condition. No slip boundary condition was applied at the channel walls. Multiblock structured meshes with around 10 million cells were used, with near-wall refinement. Based on the finite volume method, conservation of Navier–Stokes momentum in the device is described by Eq. S1 in the following:

$$\frac{\partial}{\partial t}\left(\rho\vec{V}\right)+\nabla\cdot\left(\rho\vec{V}\vec{V}\right)=-\nabla P+\bar{\bar{\tau}} \qquad \text{(Eq. S1)}$$

The conservation of mass is described by the continuity equation, Eq. S2:

$$\frac{\partial \rho}{\partial t} + \nabla \cdot (\rho \vec{V}) = 0 \qquad \text{(Eq. S2)}$$

ρ is the fluid density, $\vec{V}$ is the velocity vector, P is pressure, $\bar{\bar{\tau}}$ is stress tensor, t is time and ∇ is the standard spatial grad operator. The physical properties of water were applied to the fluids participating in the simulation (density ρ=1000 kg/m^3 and dynamic viscosity μ=10^{-3} kg/m/s). A diffusion coefficient D=10^{-10} m^2/s was used for the fluids in the simulations. In addition, for fluid mixing calculation, water A and B were set as 1 and 0, respectively. A second-order limiting scheme was used for solving the species diffusion. The convergence limit for mass fraction was set to 10^{-6} and the simulations were run for ≈ 2000 times until the flow reached the outlet.

The channel Reynolds number and the *Dean* number

The hydrodynamic force was recognized as the inertial aligning, *i.e.*, self-focusing of the particles, where randomly dispersed particles in the channel center migrate laterally along the streamlines to equilibrium positions around the channel walls under the influence of inertial lift forces (F_L, consists of the shear-induced lift force F_{LS} to push cells toward the wall, and the wall-induced lift force F_{LW} to drive cells away from the wall), *Dean* drag force (F_D, promoting specific aggregation of different sized cells), and Saffman lift force ($F_{L\Omega}$, hydrodynamic force arisen from rotation of the cells).[4-5]

Usually, F_L is given in the following, with a_p, ρ, U, and f_L as the diameter of particle, the fluid density, the maximum velocity in the channel, and the lift

coefficient respectively, and D_h=2HW/(H+W) as the hydraulic diameter. Obviously, inertial lift force is extremely sensitive to the size of the particle ($F_L \propto a_p^4$).

$$F_L = \frac{\rho U^2 a_p^4}{D_h^2} f_L \quad \text{Eq. (S3)}$$

F_D can be expressed in the following, with U_D=1.8×10^{-4}$De^{1.63}$ as the transverse velocity.

$$F_D = 3\pi\eta U_D a_p \quad \text{Eq. (S4)}$$

Dean number, *De*, is given by:

$$De = Re\sqrt{\frac{D_h}{2R}} = \frac{\rho U D_h}{\eta}\sqrt{\frac{D_h}{2R}} \quad \text{Eq. (S5)}$$

Re, Reynolds number, is a dimensionless quantity that describes the type of flow arising from effects of viscosity, U is the flow velocity in the channel, η is the dynamic viscosity of the fluid, and R is the curvature radius. *De* characterizes the magnitude and qualitative features of *Dean* flow.[6] Actually, $F_{L\Omega}$ nearly fails to work due to low AR microchannels. F_L and F_D, however, play dominant roles in competition of keeping particles approaching the microchannel wall and directions of the two forces are perpendicular to the main flow.[7] The former is mainly responsible for prompting cells to their equilibrium positions, and the latter from *Dean* flow is always focusing on the acceleration of single-cell aligning process.

Design and fabrication of microfluidic device

The one-stop horizontal single-cell sampling microchip (OS-Chip) consisted of a polydimethylsiloxane (PDMS) fluidic layer and a glass slide (Figure 2G). PDMS fluidic layer with an enhanced spiral channel (D3-ESC) segment of six loops (width:

300 μm, height: 30 μm, total length: 20.60 cm, volume: 1.67 μL), a omnipotent purifier (OP) segment (width: 400 to 980 μm, height: 30 μm, length: 1.04 cm, volume: 0.36 μL), a LIF View Finder (LIF-VF) segment (width: 20 μm, height: 30 μm, length: 0.82 cm, volume: 0.050 μL), and a horizontal capillary (HC) segment (length:1000 μm, 186 μm O.D., 50 μm I.D.).

The microfluidic device was fabricated utilizing standard soft lithography with PDMS via the following steps. (1) AutoCAD software was used to design the patterns of the microchannels. (2) We printed microchannels on transparent films (MicroCAD Photomask, Ltd., Suzhou, China) to form a photomask. (3) The mold was constructed through one step under UV light using SU8-2050 photoresist (Microchem, MA, USA) on mask aligner (7 mW/cm^2, CETC, China). (4) The mold was exposed to trimethylchlorosilane vapor for 60 min before fabrication of the microfluidic chip. Well-mixed PDMS pre-polymer [RTV 615 A and B (10:1, w/w)] was then poured onto the mold placed in a Petri dish to yield 3×10^3 μm-thick PDMS replica. After degassing, the mold was baked at 80°C for 30 min. The PDMS replica was then peeled off the mold. Afterwards, oxygen plasma treatment was used to make the glass and PDMS surface hydrophilic. The plasma treatment provided a strong and irreversible bonding between them and leakage was effectively avoided. Finally, the device was ready to use after baking at 80°C for 2 h.[6, 8-9]

LIF Detector Construction

LIF system was established according to the literature with minor

modifications. [10] A 473 nm diode-pumped solid-state laser (20 mW, Lasever, Ningbo, China) was employed as an excitation source. After passing through a band-pass filter (461–479 nm, HB Optical Technology, Shenyang, China), the laser beam was reflected by a dichroic mirror (500 nm, HB Optical Technology) and focused into the capillary channel by a microscope objective (40×, numerical aperture 0.6, Beijing Dayueweijia Technology, China). The resulting fluorescence was collected and collimated by the same objective. When transported through the same dichroic mirror and a band-pass filter (512.5–557.5 nm, HB Optical Technology), the collimated fluorescence was reflected by a mirror to a pinhole (0.4 mm). Behind the pinhole, a photomultiplier tube (PMT) with a frequency bandwidth of DC to 10 kHz (H10722-20, Hamamatsu Photonics, Japan) was used to capture the collected fluorescence and transform them into an electronic signal, and then, the output signal from PMT was obtained using a USB-6009 data acquisition card (a maximum sample rate of 48 kS/s, National Instruments, TX, USA). The data were read and processed offline with an in-laboratory program on LabVIEW (National Instruments).[10]

Coefficient of focusing (F_{co})

A confocal factor $F_{co}=a_p/W_T$ was defined as the ratio of the particle diameter (a_p) to normalized trajectory-width (W_T), where n is the number of a set of fluorescence images (≥100) repeatedly captured at the same position from the same particle focusing test, W_{Ti} is the sum of trajectory-width at each datum point (i). F_{co} is a measure of the particle focusing within the region of interest.

$$W_T = \frac{1}{n}\sum_i^n W_{Ti} \quad \text{Eq. (S6)}$$

F_{co}=1 denotes complete focusing (conformation of single-cell stream), while F_{co}=0 corresponds to no focusing at all. If the trajectory-width is less than or equal to twice of the particle diameter, *i.e.*, $F_{co}\geq 0.5$, an excellent focusing is observed. $F_{co}<0.5$ is not a reasonable focusing.

Evaluation of the Purifier

Isolated Purifier contains Inlet 1 connecting D3-ESC (a in Figure S12), Inlet 2 (b in Figure S12), Outlet 1 (c in Figure S12), and Outlet 2 (d in Figure S12). The Inlet 1 was used for the introduction of artificial samples, *e.g.*, blood, fluorescein solution, cell suspension, *etc.* Inlet 2 introduced the rinsing solution, *e.g.*, PBS or ultrapure water. Outlet 1 was used for waste discharging, and Outlet 2 was used to connect the horizontal capillary (HC) for sampling and analyzing of the aligned single cells.

Residual rate was used for the evaluation of the purifier performance by introducing different concentration of AuNPs solution from TC and PBS from Inlet 2, by using the following equation.

$$Residual\ rate = \frac{N_{outlet2}}{N_{ESC}} \quad \text{Eq. (S7)}$$

$N_{outlet2}$ is the count of AuNPs in the collected solution from Outlet 2; N_{ESC} is the count of AuNPs in Inlet 1 connecting ESC.

Sample loss rate was used for evaluating the loss of sample in the purifier under different flow rate ratios of Inlet 1 and Inlet 2. Inlet 1 introduced cells in DMEM medium and Inlet 2 introduced PBS. The sample loss rate was expressed in the

following equation.

$$Sample\ loss\ rate = 1 - \frac{n_{c2}}{n_{I1}} \quad \text{Eq. (S8)}$$

n_{c2} was the count of cells in the collected solution from Outlet 2, while n_{I1} was the count of cells introduced into Inlet 1.

The shear stress

The shear stress ($\tau_{(cell)}$) was calculated by using the following equation:

$$\tau_{(cell)} = \frac{6Q\eta}{h^2 w} \quad \text{Eq. (S9)}$$

$$Q=UA \quad \text{Eq. (S10)}$$

Q was the volumetric flow rate, η was the dynamic viscosity, h was the channel height, and w was the width. U was the linear flow rate and A was the cross sectional area of the microchannel or microchamber.[11-12]

Operating procedures

Before operation, the microfluidic platform was washed sequentially with 75% ethanol for 1 h, PBS for 0.5 h, and sterile water for 0.5 h at flow rates of 100 μL/min. The trypsinized cells were divided into two parts, one for single cell analysis subsequently without any extra treatment, and the other for cell counting after washing three times with PBS and resuspended. Unprocessed cell samples and rinsing solution (PBS) were driven by two syringe pumps respectively into the one-stop horizontal single-cell sampling in capillary (COLE-PAEMER, 2000 μm×190 μm) connecting with ordinary stainless steel tube (25 G). The aligned cells from OS-Chip

were introduced to ICP-MS through a horizontal capillary (Polymicro TECHNOLOGIES, length: 1000 μm, 186 μm O.D., 50 μm I.D.) connected to the Outlet 2 of the device.

Cell viability

MTT assay was designed to detect the cell viability. After culturing the cells with specified concentration of metals, the medium was removed, and the cells were incubated with MTT solution (0.5% (m/v)) for 4 h. Then the MTT solution was removed and DMSO was added allowing for vibration for 10 min, and the absorbance was measured utilizing the microplate reader at 570 nm.[13]

Data processing

For the purpose of differentiating the single cell events from background signals, an iterative algorithm method and Gaussian fitting were adopted for data analysis.[14] The mean and three times standard deviation (3σ) were calculated for all the data, and the obtained value below 3σ above the mean were recalculated with the same algorithm until no data points were higher than the sum of 3σ and average signal value.[15] The final value was set as a threshold, and all spikes with an intensity higher than this threshold value were collected and considered as the cellular events, while those below the threshold were treated as the cellular backgrounds.[16]

To ascertain the concentration of oxaliplatin in the sample solution, we employed the standard curve method, as depicted in Figure S21A. The signal from the ^{195}Pt

isotope, derived from the sample solution, was integrated into the working curve using the atomic spectroscopy mode of ICP-MS. This approach facilitated the verification of oxaliplatin's presence in the sample solution.

For the quantification of oxaliplatin in individual cells, we utilized a standard curve method, illustrated in Figure S21B. Employing a time-resolved mode of ICP-MS, the ^{195}Pt isotope signal from a single cell, obtained from a cell sample, was incorporated into the working curve. Given that the mass fraction of Pt in OXA is approximately 49%, the concentration of OXA in a single cell could be determined. By considering the cells as spheres with an average diameter of 15 μm, the uptake of oxaliplatin by cells from various cell line sources could be calculated.

Different detection parameters

The ^{197}Au signal from Au nanoparticles serves solely for cell counting and calculating the detection system's efficiency. Following the uptake or capture of Au nanoparticles by individual model cells, the ^{197}Au isotope signal within these cells is detected using the time-resolved mode of ICP-MS, facilitating accurate cell quantification.

It is crucial to note that the ^{197}Au signal of BioNPs is not actively monitored and collected during the actual sample detection due to limitations in the time-resolved mode of ICP-MS, which does not support simultaneous acquisition of two-element signals in high-throughput sampling scenarios. Therefore, only the ^{195}Pt isotope signal

is collected by ICP-MS during the experimental phase.

The ^{195}Pt isotope signal is instrumental in exploring oxaliplatin uptake in single cells from different tumor types. Monitored through the time-resolved mode of ICP-MS, the ^{195}Pt isotope signal allows for the quantification of oxaliplatin content within single cells based on the standard working curves of platinum element detection. (Figure S21)

In assessing the expression of PTK7 in single cells from diverse tumors, the 6-FAM fluorescence signal of BioNPs serves as a key indicator. The fluorescence intensity of 6-FAM correlates positively with PTK7 protein expression. Initially, the fluorescent signal is collected using LIF from various tumor cells, followed by the introduction of these cells into ICP-MS for platinum isotope mass spectrometry signal collection. This ensures the simultaneous acquisition of fluorescence signals and platinum mass spectra from the same single cell, facilitating the determination of oxaliplatin uptake and the corresponding PTK7 protein expression within individual cells.

Cell transport efficiency

The cell transport efficiency was calculated by comparing the number of spikes (spike frequency) for ^{197}Au isotope in a time interval of 60 s at a flow rate of 20 μL/min (*i.e.*, a sample volume of 20 μL), with the cell suspension (20 cells per μL).

In general, MCF-7 cells after exposure to 10^5 mL^{-1} of AuNPs suspension

(60.8±7.5 nm in diameter) were detected by measuring the isotope of ^{197}Au. The dwell time (t_{dwell}) of 0.1 ms, cell number density of 2.5×10^4 cell/mL were employed for our studies.

Immunofluorescence staining

After alignment and purification, collected cells were fixed by 4% polyformaldehyde, and then blocked by goat serum, followed by immunofluorescence staining with anti-EpCAM, anti-panCK, anti-CD45, the probes. The immunofluorescence results were scanned by a fluorescence microscope (Olympus, Japan).

Results and Discussion

Competition assays for BioNPs and aptamer

In order to verify the ability of the BioNPs probe to bind to the biomarker on the cell surface, the aptamer and the probe were bound to MCF-7 cells separately, and then the probe and the aptamer were added to each of them to further compare whether they could displace each other. As shown in Figure S1D, the probe can displace the aptamer, but the aptamer cannot displace the probe. This indicates that the probe has a stable binding capacity after binding to the cell.

Optimization of the single-cell alignment unit

It has been widely recognized that periodic micro-obstacle equipping in spiral channel boosts single particle/cell alignment. The authors' laboratory recently established unique spiral microchannels for the regulation of *Dean*-like secondary flow to achieve highly-efficient single-cell alignment.[17] However, higher focusing flow rate may lead to a decrease in the transport efficiency of subsequent single-cell detection. Therefore, five candidate spiral channels were employed for exploring an optimal particle focusing configuration by numerical simulation and fluorescent microparticle investigation (Figures S3, S4). Various micropillars with different sizes (length: 150, 450, 750, and 900 μm; width: 150 μm) were incorporated in the 6-loop spiral channels (D1 to D4). Firstly, numerical simulation was applied to quantitatively distinguish the fluid flows in the designated microfluidic channels. As shown in Figure S5, the fluid velocity field in *x*-axis (U_x) and *y*-axis (U_y) in D3 and D4 were more changeable than that in D1 and D2, which probably provides faster instantaneous velocity in y-axis to arise *Dean* flow readily. However, obvious

vorticose velocity distribution appeared in non-micropillar regions, which has adverse effect on the particle alignment due to the disruption of respective equilibrium position of single particles/cells. Therefore, to improve single particle alignment performance, the enhanced spiral channel (D3-ESC) was designed by arranging the enhanced curves (EC) between two micropillars. Surprisingly, more distinct flow distribution and gentle vortex were generated in spiral channel of the D3-ESC (Figure S5). It was attributed to equipped periodic wider dimensional-confinement pillars and high-curvature curves in D3-ESC, which could strengthen *Dean* drag force and assist cells/particles to align in their equilibrium position more rapidly. Moreover, wider micropillars in spiral channel was capable of reducing cell focusing flow rate,[18] which protected cells from the damage of shear stress under high flow.

For systematically investigating the effect of secondary flow on particle alignment, these five devices (D1, D2, D3, D4, and D3-ESC) were fabricated. As shown in Figure S6, poor particle alignment was observed in D1, D2, D3 and D4 under low flow conditions (*Re*=1.01, 10 μL/min). However, the tight fluorescence trajectories of 19.3 μm diameter particles through the D3-ESC configuration demonstrated that periodic wider dimensional-confinement pillars and high-curvature curves (*i.e.*, EC) can considerably improve the particle alignment even under low flow rate. This flow rate reduced damage to the cells and promoted subsequent detection efficiency.[17] We also arranged the EC in D4 configuration to investigate the influence of more extreme confinement on the performance of particle focusing performance.

Unfortunately, it was observed that the over constriction resulted in the generation of disordered trajectories of particles in the EC region (Figure S7), which was not favorable for the alignment of particles. Thus, the D3-ESC configuration was employed for the subsequent single-cell alignment/sampling.

To investigate the vortex strengthening and fluid flow profoundly, ESC was adopted as a numerical simulating model in accordance with the above flow rate. In Figure S8, quantitative comparison of nine sectional views relevant to the flow in the y-axis at diverse locations between two confinement spaces illustrated the dynamics of cross-sectional flow. In the Section 1/9 and 5 corresponding to the central region of two wider micropillars and EC, obvious *Dean* vortices were generated, which demonstrated *Dean*-like secondary flow train boosted progressive alignment to a continuous single-stream. Although the velocity (U_y) was increasing or decreasing consecutively after passing through a set of ECs and wider confinement spaces, the alternate processes of explicit dispersing (U_y<0) and then congregating (U_y>0) increase the strength of *Dean* vortices, and promote the accumulation of particles.[17]

Optimization of purification unit and comparison with centrifugation

The Purifier has 42 micro filtration-pillars (mi-FPs, with dimensions of 20 by 40 μm width by height). The pillars connected to the end of the spiral channel unit and the beginning of LIF View Finder (LIF-VF). The width of the purification unit was set within 450-950 μm, with a channel depth of 30 μm. The sample and the rinsing solution were introduced to the Purifier through the D3-ESC and Inlet 2, respectively,

and they would meet at an intersection. Actually, the width of two channels might influence the flow ratio of sample and rinsing solution, which probably determined the purification efficiency of the real sample.[19] Therefore, six configurations of purifiers were designed and constructed for identifying the most suitable intersection configuration (Figure S12). Comsol numerical simulation and fluorescein purifying test were performed under 20 μL/min of sample (concentration was set to 1 or 1 μM fluorescein solution) introduced from "a" and 40 μL/min of purifying agent (concentration was set to 0 or ultrapure water) introduced from "b" (Figures S13 and S14). The results showed that P2 configuration played a prominent role in boosting the rinsing agent to wash fluorescein through mi-FPs to Outlet 1 and to mainly distribute the target single cells to Outlet 2 as theoretically expected. In Figure S15, streamlines were directed to flow through the gaps between mi-FPs, and the gap spacing was less than the diameter of cells which may generate high resistance. This enabled the process for sifting the target cells from biomatrix containing contaminants.

Further, in Figures S16 and S17, excellent purifying performance were validated by numerical simulation and fluorescein test within a wide range of flow rate ratios in fluid from D3-ESC and Inlet 2 (20:20-20:80, μL/min). Considering that a high flow rate of rinsing agent may cause decrease on the single cell measurement efficiency[17] (Figure S17C), the flow rate ratio of 20:40 (μL/min) was employed. Significantly, this purifier exhibited less sample loss with respect to the traditional centrifugal cleaning.

Subsequently, we confirmed the purification capacity to rinse multiple sample concentrations of the biofunctionalized-nanoprobes (BioNPs) (10^5, 10^6, 10^7 probes per mL) which exhibited as the false positive interference. The TRA-ICP-MS mode (single nanoparticle mode) and "Count" were employed for evaluating purification ability for nanoparticles. One count means the sample is positive. Figures S19 clearly illustrated that the probes were not identified in the collected fluid from Outlet 1 (~0 count), which well demonstrated the effective purification capacity of the unit.

Considering the excellent performance for sample purification, further experiments were conducted to evaluate the purification capability in the presence of trypsinized cell medium, OXA containing medium (0, 0.05, 0.1, 0.15, 0.2 μM), whole blood with 10^6 cells per mL. The spectrum mode and concentration were employed for evaluating purification ability for molecular medicine. As shown in Figure S20, nanoscale interferents such as vesicles were effectively removed. Further, compared with the cell density at the Inlet 1, the cell density collected from the Outlet 2 was ca. three times higher. In addition, no ^{195}Pt isotope was observed in the collected sample from Outlet 2 after purifying the OXA containing medium (Figure S21). Further, whole blood with different Hct (2.5, 5, 7.5, 15 and 45%) containing 10^6 MCF-7 cells/mL were purified successfully and >97% cells were maintained (Figures S22 and S23).

Centrifugation methods have become one of the most common methods for preparing samples for analysis. However, for cell samples, centrifugation may lead to

cell loss, reduced cell viability, and extravasation of target elements from the cells. Therefore, microspheres and real cell samples were employed to compare the centrifugation method with this microfluidic method. In Figure S17C, the loss rate of microspheres after three times centrifugations was ~30%, while in microfluidic chips, the loss rate was only about 3% (20:40 μL/min). For real cells, as shown in Figure S17D, with the increase in centrifugation steps, the number of cells was gradually lost and the cell viability was gradually decreased. In contrast, as shown in Figure S17D and S25, using microfluidic methods, the cell retention rate was at 95.3%, and the cell viability was at 98.9%.

Optimization of cell number density and laser strobing

It is a significant requirement for time-resolved single cell measurement that each ICP-MS spike corresponds to each LIF burst from a single cell event. That is the cells in the suspension are needed to be well-separated spatially and temporally. Although the single-cell throughput could be increased by improving the cell density of sampling, an instantaneous spike may probably correspond to several cells, because higher density of cells may cause more than one cells to be detected in an individual sampling period. The calculation of cell spacing indicated that the average interval time between two adjacent cells is 3.31×10^4 ms, 3.31×10^3 ms, 3.31×10^2 ms, 1.32×10^2 ms, 33.1 ms, 3.31 ms, and 0.33 ms corresponding to cell density of 10^2, 10^3, 10^4, 2.5×10^4, 10^5, 10^6, and 10^7 per mL, respectively. The time interval of 132 ms (2.5×10^4 cell

per mL) provided subsequent cellular temporal resolution (Figure S31). Therefore, a cell number density of 2.5×10^4 cells/mL was adapted for the ensuing studies. Moreover, as shown in Figures S28 to S30, we obtained the response values of LIF (6-FAM, 494 nm) from single probes for quantifying PTK7 expression level.

Unification of single-cell LIF-ICP-MS signals

Each individual cell undergoes introduction into the ICP-MS subsequent to its traversal through the LIF detector, thereby inducing a temporal delay across the two detectors. Nevertheless, since single cells manifest distinct aerosol characteristics upon passage through the nebulizer preceding their introduction into the ICP-MS, an inherent stochasticity arises, resulting in a non-uniform temporal disparity.[20] Consequently, the time lapse from the moment a cell undergoes LIF analysis to its subsequent detection by ICP-MS becomes indeterminate. We endeavored to maintain experimental conditions with maximal consistency. However, owing to the impact of diverse factors such as subtle fluid perturbations, the pulsatile operation of the syringe pump, and the responses of LIF and ICP-MS, it became imperative to calibrate the temporal synchronization of the two instruments for different cell lines to align with the 2D data for each individual cell.

Taking into account transfer efficiency, the volume of data acquired from LIF surpasses that from ICP-MS for an identical set of single-cell data. In contrast to ICP-MS, LIF demonstrates superior single-cell detection efficiency (100%)

attributable to its high-frequency detection capabilities. It is pivotal for the precise correction of 2D data. Therefore, we benchmarked the time axis of the single cell signal produced by ICP-MS rather than the time axis of the signal produced by LIF. This ensures that each identified single cell has 2D signal data for both mass spectra and fluorescence. In this study, we established the validation method through programming-operation-based Python,[21] as described in the following formula: Ct = L_x - I_y. L is representative of the time corresponding to the peak of the single-cell LIF spike (x = 1, 2, 3⋯n, where n is the total number of LIF spikes), while I denotes the time corresponding to the peak maximum of single-cell ICP-MS spikes (y = 1, 2, 3⋯m, where m is the total number of ICP-MS spikes). Upon computation of all Ct, a frequency distribution graph is generated, and the X_c value at the highest frequency is considered as the Ct. Figures 3H and S29 presents a mean value of the Correction times (Ct) of 26.080 ± 0.449 s for a single cell from diverse cell lines to traverse through LIF and ICP-MS. The results indicate that within this range, no concurrent cell spikes were identified on either the left or right sides. Subsequently, the single-cell 2D signal, post-screening based on the time difference, is depicted in Figure 3H, ensuring subsequent 2D data analysis for the corresponding LIF and ICP-MS detection of the same single cell.

Applications in real samples

In the device, the shear stress on cells were very small (0.043 dyne/cm^2, Figure 2I). The MCF-7 cell suspension was collected from Outlet 3 (with a sample loss rate

of 6.28±1.06%, n=5) and followed by cell culture for 48 hours. During this period, the cells grew by adherence and proliferation (Figure S25). It indicated that the purifying process had no damage on the cell activity. [20]

For procuring single-cell analysis of rare CTCs, adequate high cell measurement efficiency was needed. Multiple concentrations of MCF-7 cells exposed by standard AuNPs (60.8±7.5 nm, 2×10^5 AuNPs/mL) were used for evaluating single cells measurement efficiency. Individual cells were isolated in the OS-Chip followed by introducing into ICP-MS and detecting ^{197}Au isotope (Figure S27). A series of steady transient signals for single cells illustrated its favorable stability in the generation of single-cell stream. The measurement efficiency was derived to be 90.6±7.6% (n=5, with confidence limit of 95%). In general, it clearly indicated that the present approach profits prominently single-cell analysis, with a significant improvement on the measurement efficiency from 1% for conventional approaches to >90% in this study (Table S2).[17] Furthermore, we measured the single-probe signal by the optimum of data filtering in our previous study based on iterative algorithm.[10] In Figures S28 and S30, RFU=0.034 and cps=44876.61 were obtained as single-probe response values of LIF and ICP-MS for the evaluation of labeling number of probes on an individual cell.

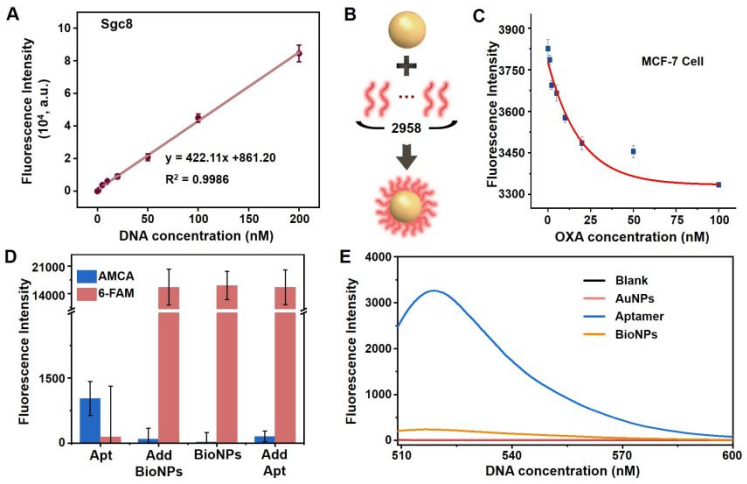

Figure S1. (A) The standard working curves of 6-FAM labeled Sgc8. (B) The number of aptamers loading on each AuNP of BioNPs. (C) The variation of fluorescence intensity with OXA concentration (Fitting curve: y=33337.42+4419.29×exp(x/18.96)). (D) When the aptamer and probe are bound to the cell separately, the BioNPs can displace the aptamer, while the aptamer cannot displace the probe. (E) Fluorescence spectrum of Blank (water), AuNPs, Aptamer (Sgc8-6-FAM), and BioNPs in aqueous solution at λ_{ex} = 494 nm. The BioNPs probe quenches the fluorescent group 6-FAM compared to the aptamer. the BioNPs probe binds to the cell and restores fluorescence. This may occur because the Sgc8 aptamer has 51 base pairs and the nucleic acid chain with the fluorescent group stretches and moves away from the gold nanoparticle surface when binding to the cellular protein, allowing the fluorescence to recover. The data indicate mean ± standard deviation (SD). Three independent groups to be tested by using biological replicates (n = 3) were used for each data point.

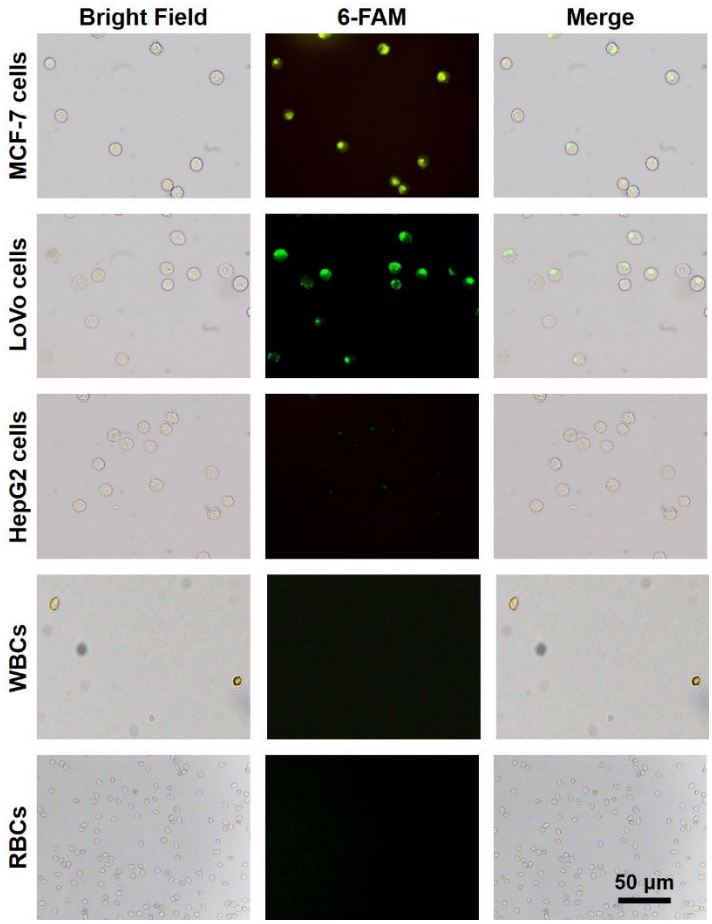

Figure S2. Representative fluorescence images of the cells after decorating with BioNPs nanoprobes, *i.e.*, MCF-7 cells, LoVo cells, HepG2 cells, WBCs, and RBCs.

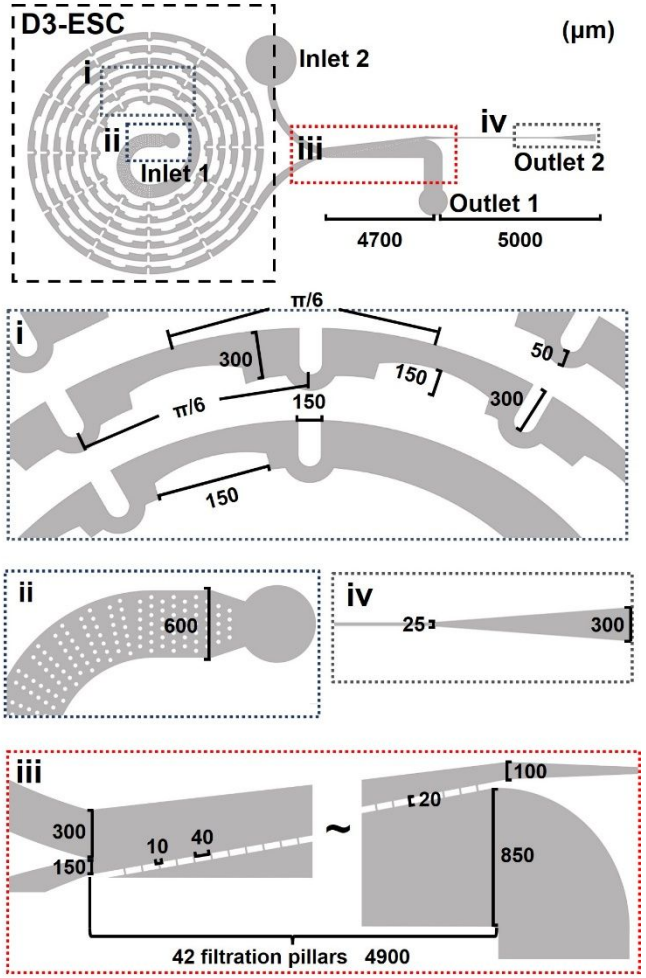

Figure S3. Schematic diagram and design of the D3-ESC configuration. The device consists of an ultralow-aspect-ratio (AR) spiral microchannel with 6 loops, a compendious purifying channel, a LIF View Finder, two inlets and two outlets. The main microchannel structure is 300 μm in width and 30 μm in height. The distance between two adjacent loops is 300 μm. The spiral channel was designed with sequentially arranged wider micropillars in the microchannels. The amplifying images show detailed design parameters of the devices. i, ii, iii, and iv, represent the observed regions in the devices.

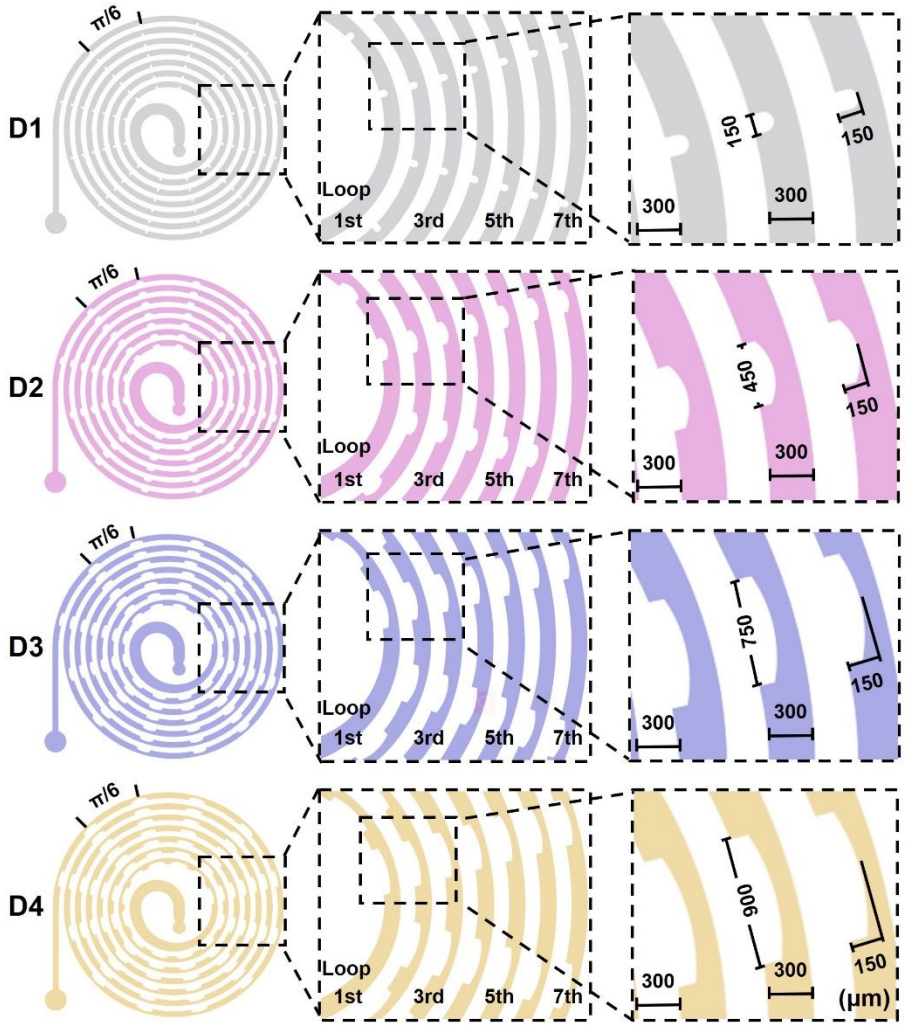

Figure S4. Schematic diagram and design of the four microfluidic devices, D1-D4. Each device consists of a low-aspect-ratio (AR) spiral microchannel with 7 loops, one inlet and one outlet. The main microchannel structure is 300 μm in width and 30 μm in height. The distance between two adjacent loops is 300 μm. D1 to D4 were designed with sequentially arranged micropillars with different sizes in the microchannels. The amplifying images show detailed design parameters of different devices.

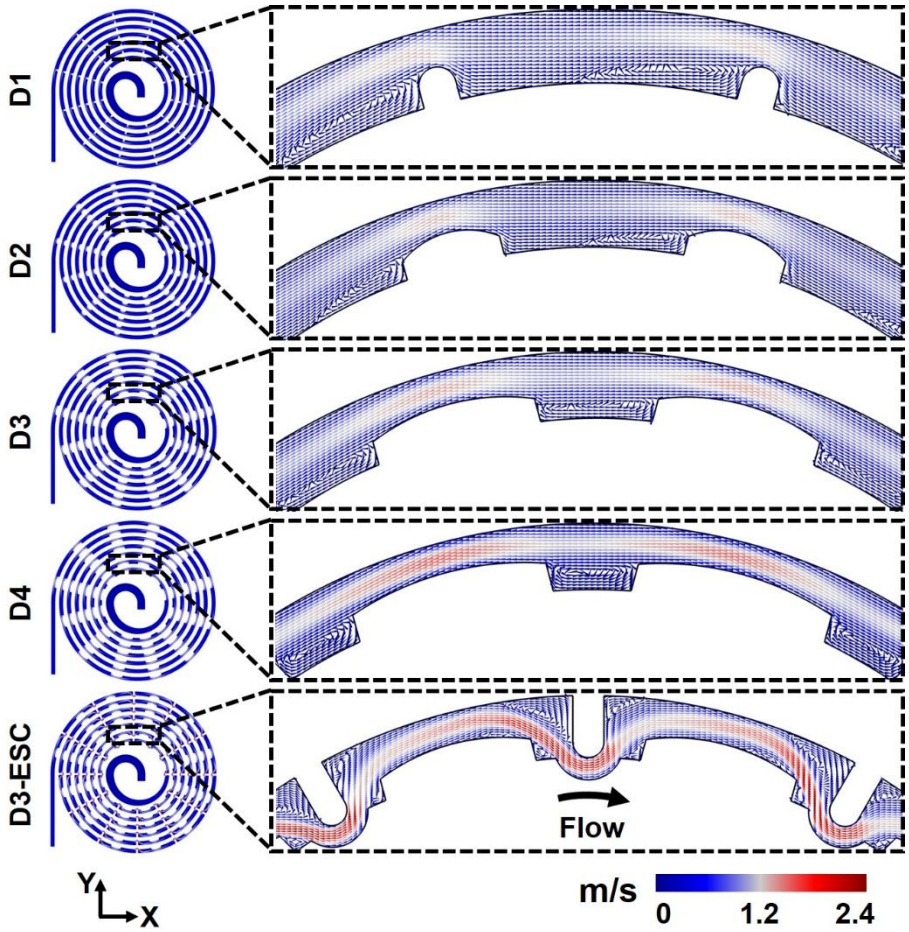

Figure S5. Representative fluid velocity field of the inertial flow (flow rate: 10 μl/min, *Re:* 1.01) in the microfluidic configurations of D1, D2, D3, D4 and D3-ESC.

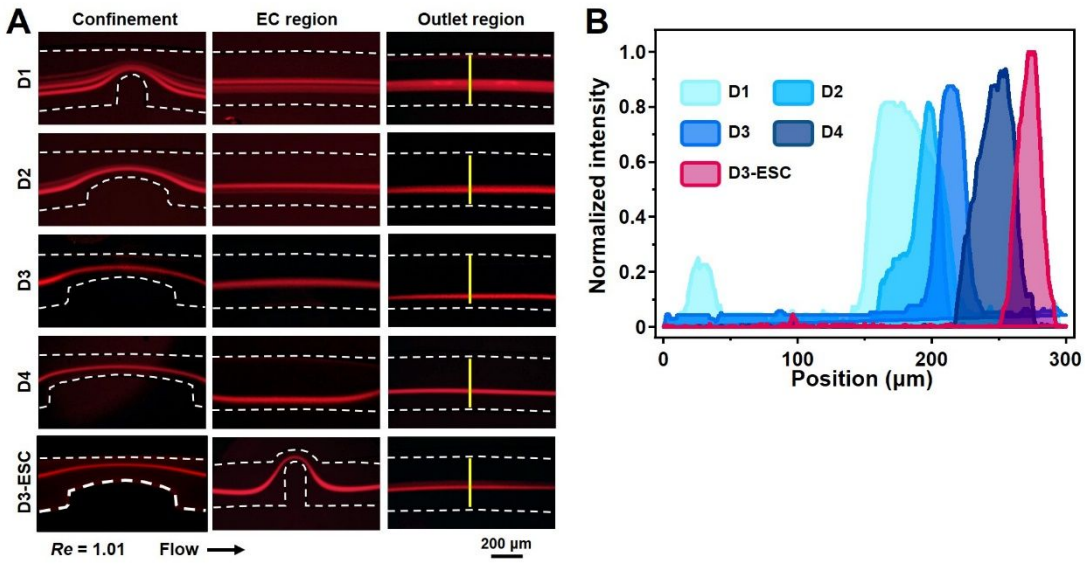

Figure S6. (A) Trajectories of the fluorescent particles (19.3 μm in diameter) in different regions of ESC under *Re* of 1.01 (Flow rate: 10 μL/min). The yellow lines were used to analyze single cell alignment at the same transverse positions. (B) Fluorescence intensity analysis in diverse spiral channels.

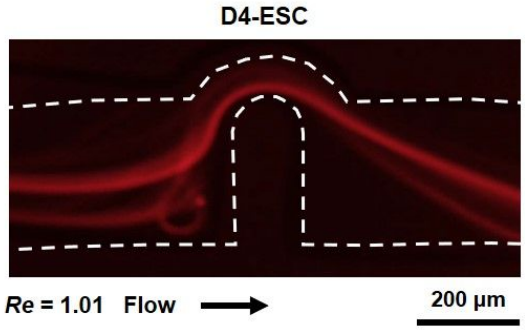

Figure S7. The trajectories of fluorescent particles (19.3 μm in diameter) in the region EC of D4-ESC configuration. The inevitable vortexes caused by the overly constricted structure leads to the disordered particle trajectories.

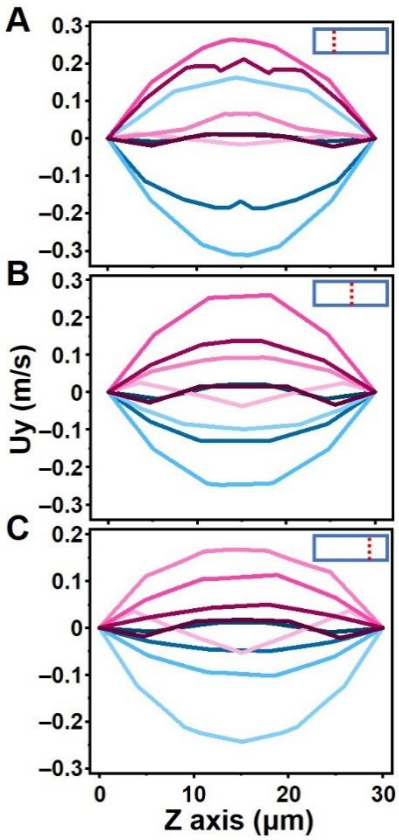

Figure S8. A) Quantitative comparison of nine sectional views relevant to the flow in the y-axis at diverse locations between two confinement spaces for illustrating the dynamics of cross-sectional flow in Figure 2A. The results were obtained from one quarter (A), two quarters (B), three quarters (C) of each cross section respectively, as indicated in the upper right corners of each figure. Although velocity (U_y) is increasing or decreasing consecutively after passing a set of HcCs and wider confinement spaces, the alternate processes of explicit dispersing (U_y<0) and then congregation (U_y>0) increase the strength of *Dean* vortices, and promote alignment of the particles.

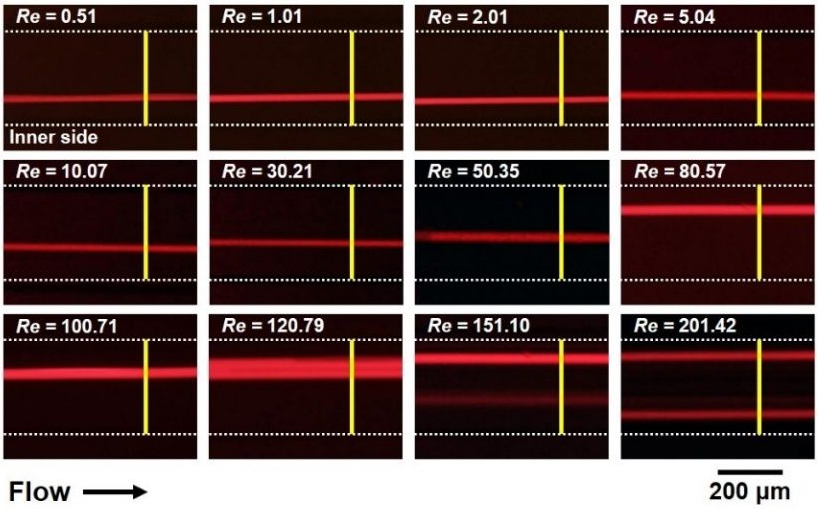

Figure S9. Trajectories of the fluorescent particles (19.3 μm in diameter) in the region at the end of D3-ESC under different *Re* of 0.51, 1.01, 2.01, 5.04, 10.07, 30.21, 50.35, 80.57, 100.70, 120.80, 151.10, and 201.40, corresponding to flow rates of 5, 10, 20, 50, 100, 300, 500, 800, 1000, 1200, 1500, and 2000 μL/min. The yellow lines were used to analyze single cell alignment at the same transverse positions. The analytical results were listed in Figure S10.

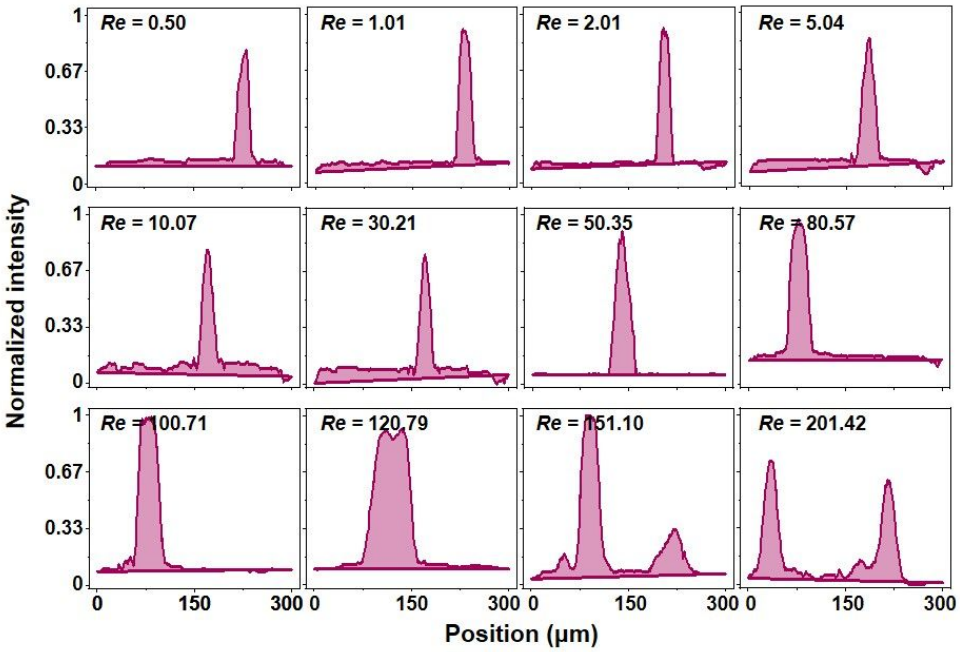

Figure S10. Fluorescence intensity analysis under different *Re* of 0.51, 1.01, 2.01, 5.04, 10.07, 30.21, 50.35, 80.57, 100.70, 120.80, 151.10, and 201.40, corresponding to flow rate of 5, 10, 20, 50, 100, 300, 500, 800, 1000, 1200, 1500, and 2000 μL/min.

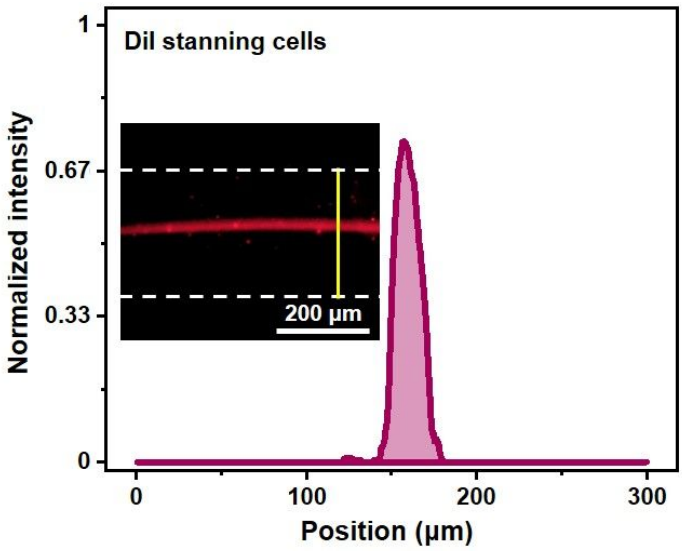

Figure S11. The cell focusing evaluation. The trajectories of MCF-7 cells staining Dil fluorescent probe in the region at the end of D3-ESC under the inertial flow condition (*Re:* 0.51, flow rate: 5 μL/min). The yellow lines were used to analyze single cell alignment. Fluorescence intensity analysis of the fluorescent cell trajectories corresponding to the yellow line.

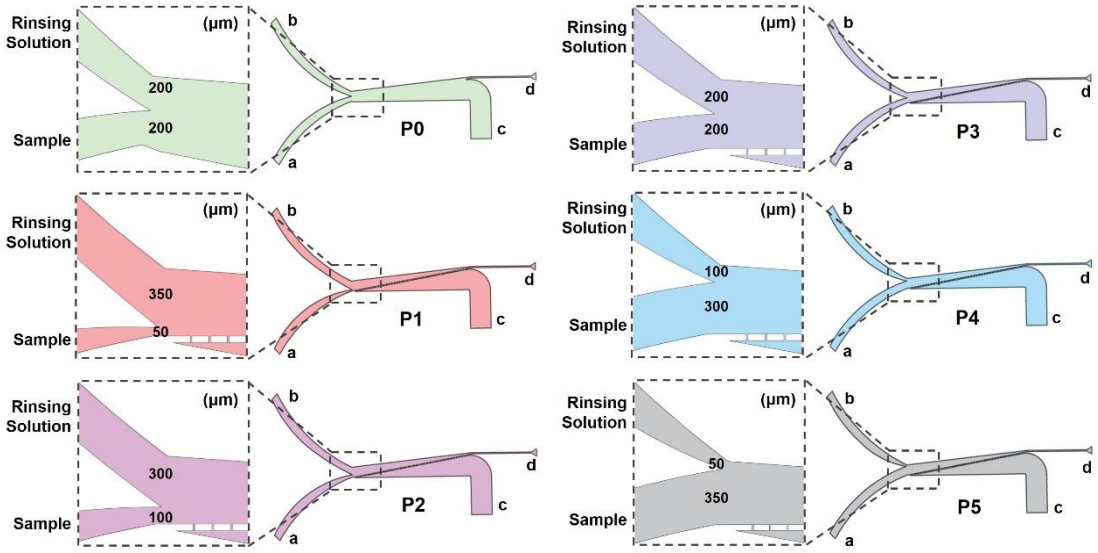

Figure S12. Schematic diagram and design of the five microfluidic purifiers (P0, P1, P2, P3, P4, P5). a, b, c, d represent Inlet 1, Inlet 2, Outlet 1, Outlet 2 respectively.

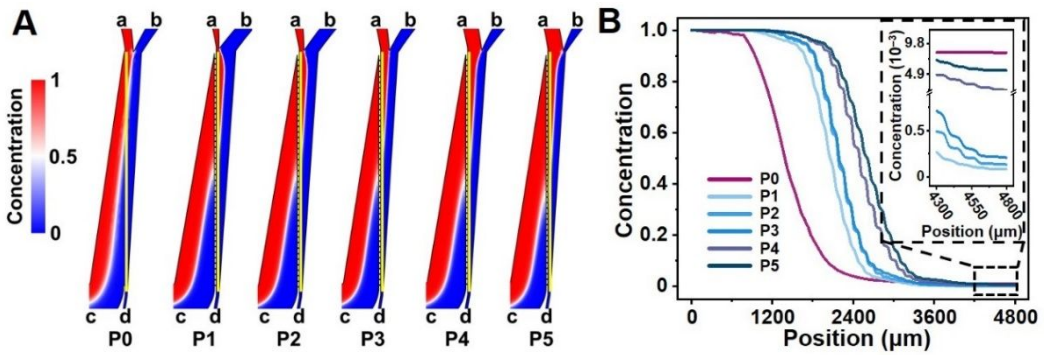

Figure S13. (A) The simulated image of concentration gradient formation in the devices (P0, P1, P2, P3, P4, P5) under flow rate ratio of 20 μL/min to (Inlet 1) to 40 μL/min (Inlet 2). The yellow lines were used to analyze the concentration gradient distributions at the same transverse positions. The analytical results were given in Figure S13B. a, b, c, d represent Inlet 1, Inlet 2, Outlet 1, Outlet 2 respectively. (B) Evaluation of purifying effect with intersection structure of the six designed purifiers with Comsol simulation (flow rate: 20 μL/min in Inlet 1 and 40 μL/min in Inlet 2).

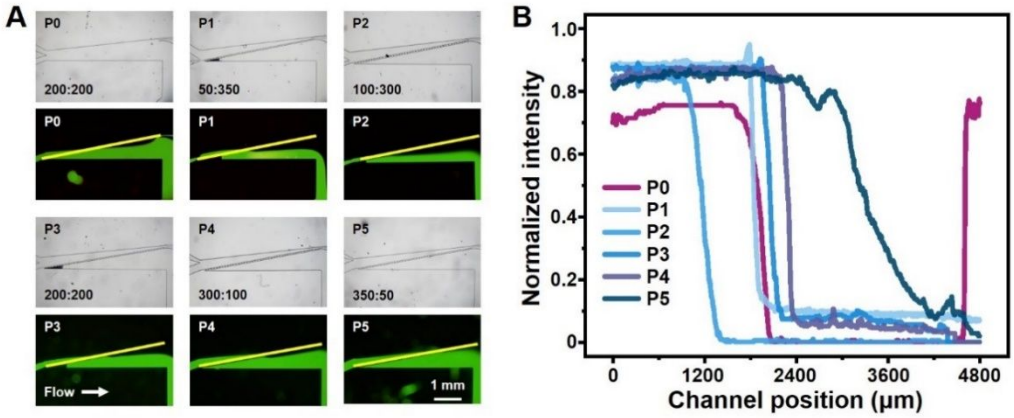

Figure S14. (A) The fluorescent images of concentration gradient formation in the six microfluidic purifiers (P0, P1, P2, P3, P4, P5) under flow rate ratio of 20 μL/min to (Inlet 1) to 40 μL/min (Inlet 2). The yellow lines were used to analyze the concentration gradient distributions at the same transverse positions. The analytical results were given in Figure S14B. (B) Evaluation of purifying effect with channel width of the five designed purifiers with real sample investigation (flow rate: 20 μL/min in Inlet 1 and 40 μL/min in Inlet 2).

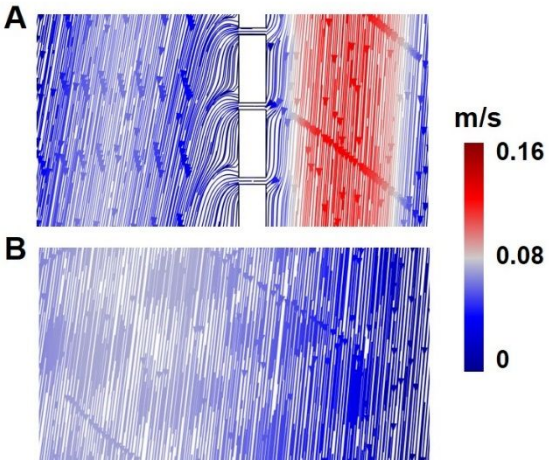

Figure S15. The simulated hydrodynamic results in P2 (A) and P0 (B).

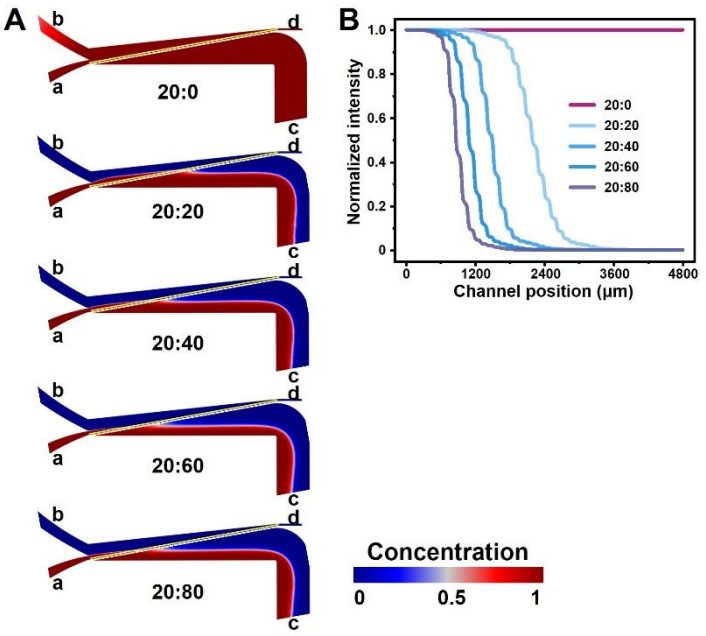

Figure S16. (A) The simulated image of the concentration gradient formation in P2 purifier under different flow rate ratios of 20:0, 20:20, 20:40, 20:60, 20:80 (Inlet 1:Inlet 2). The yellow lines were used to analyze the concentration gradient distributions at the same positions. The analytical results were given in Figure S16. (B) Evaluation of purifying effect in P2 purifier under different flow rate ratios of 20:0, 20:20, 20:40, 20:60, 20:80 (Inlet 1:Inlet 2).

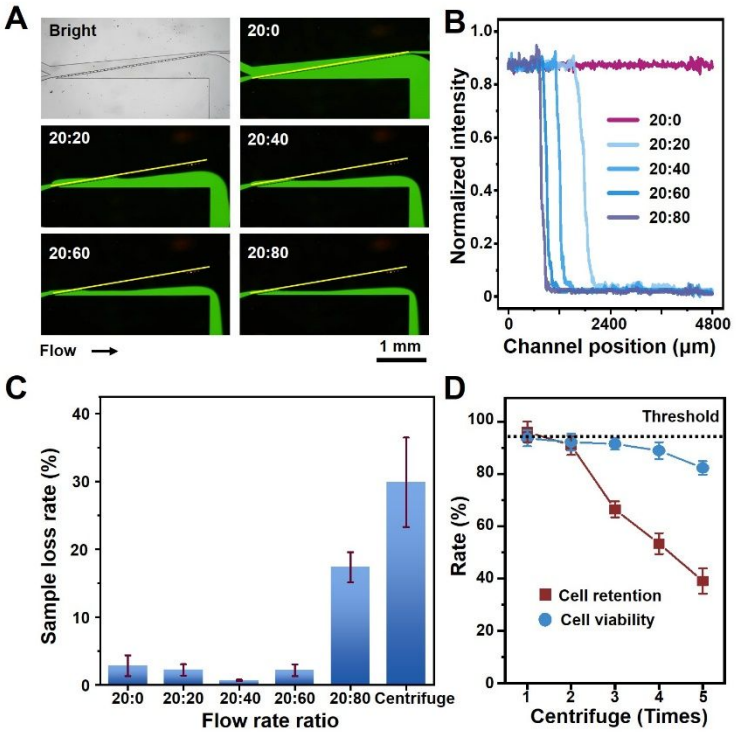

Figure S17. (A) The fluorescent images of concentration gradient formation in P2 under different flow rate ratios of 20:0, 20:20, 20:40, 20:60, 20:80 (Inlet 1:Inlet 2, μL/min). The yellow lines were used to analyze the concentration gradient distributions at the same transverse positions. (B) The analytical results were given in Figure S17A. (C) Sample loss rate at various flow rate ratio of Inlet 1:Inlet 2 (μL/min) against the result achieved by centrifugation. (D) Retention rate and cell viability of MCF-7 cells after multistep centrifugation (10^6 per mL). The threshold refers to the cell retention rate of 95.3% ± 2.6% for the microfluidic purification unit. Three independent chips prepared by using biological replicates (n = 3) were used for each data point.

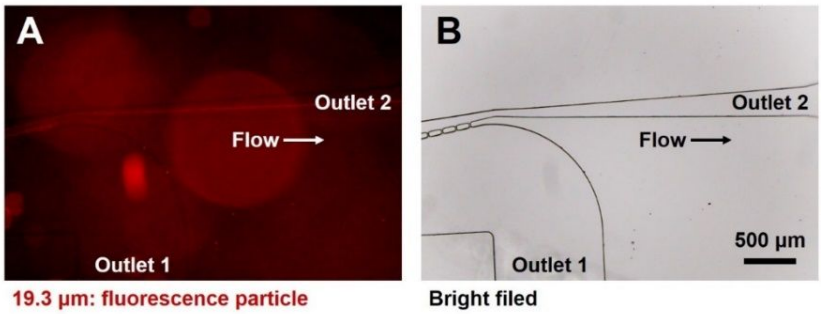

Figure S18. The trajectories of 19.3 μm fluorescent particles (A) and bright filed in the region of Outlet 2 (the flow rates at Inlet 1 and Inlet 2 were 20 μL/ min and 40 μL/min, respectively).

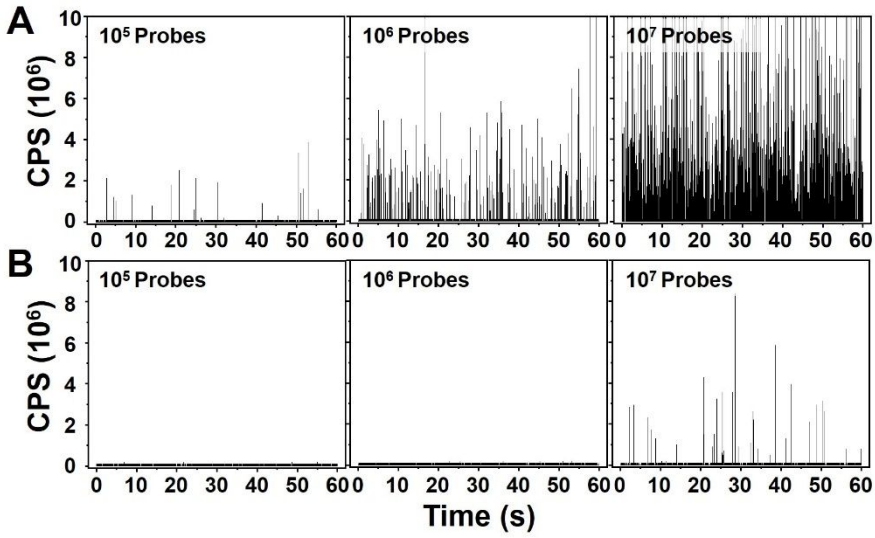

Figure S19. ICP-MS temporal profile of ^{197}Au isotope spikes of BioNPs solution collected from Outlet 1(A) and Outlet 2 (B) of the microfluidic device for the evaluation of the purifying performance.

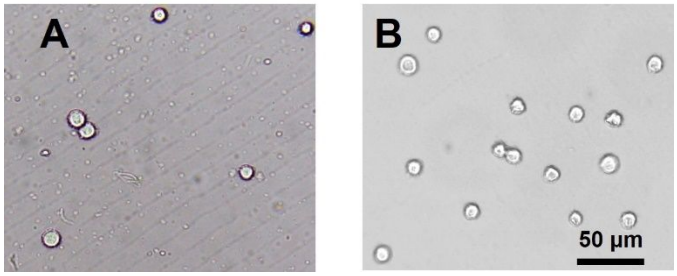

Figure S20. Evaluation of purifying performance using trypsinized medium containing (1.01 ± 0.19) × 10^6 MCF-7 cells per mL and massive vesicles (A) and collected from Outlet 2 after purification (B, containing (2.98 ± 0.36) × 10^6 cells per mL). After purification, massive vesicles in trypsinized medium were removed, and the cell number was concentrated by about three times.

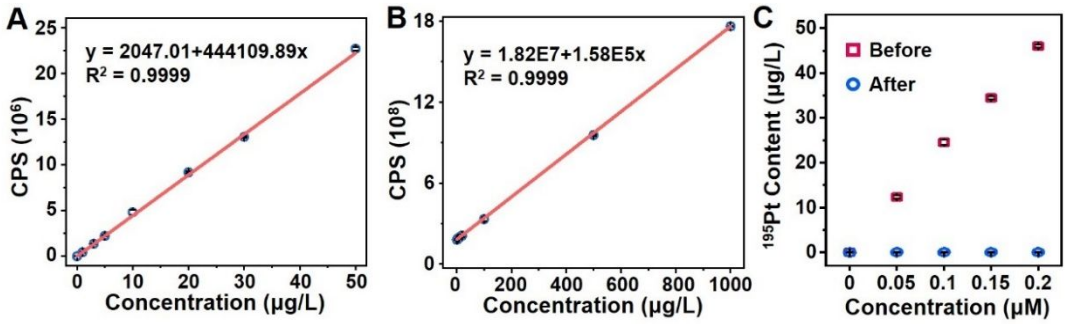

Figure S21. The standard working curves for Oxaliplatin (OXA) in ICP-MS in mass spectrum mode (A) and TRA mode (B). (C) Evaluation of the purifying performance of the purifier by using medium containing OXA and collected from Outlet 2 after purification. The data indicate mean ± standard deviation (SD). Three independent groups to be tested by using biological replicates (n = 3) were used for each data point.

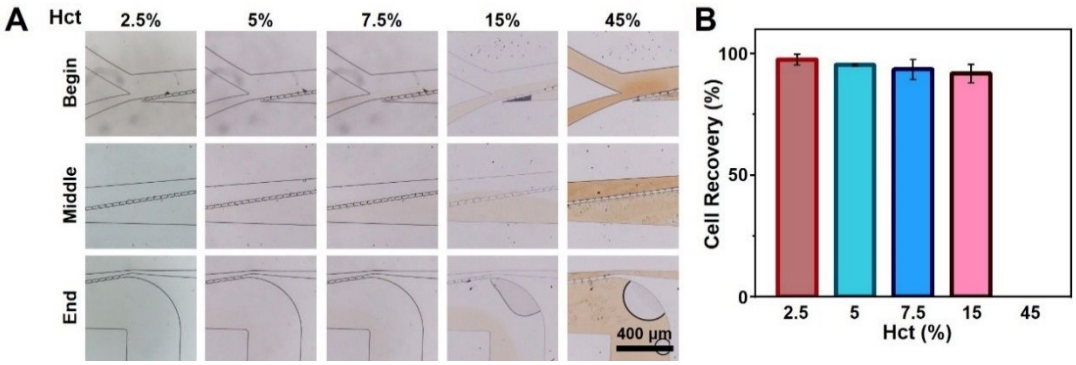

Figure S22. (A) Evaluation of purifying performance using different Hct (2.5%, 5%, 7.5%, 15%, 45%) of whole blood containing rare tumor cells (10^6 cells per mL). (B) Cell recovery of different Hct (2.5%, 5%, 7.5%, 15%, 45%) of whole blood after purification. The data indicate mean ± standard deviation (SD). Three independent groups to be tested by using biological replicates (n = 3) were used for each data point.

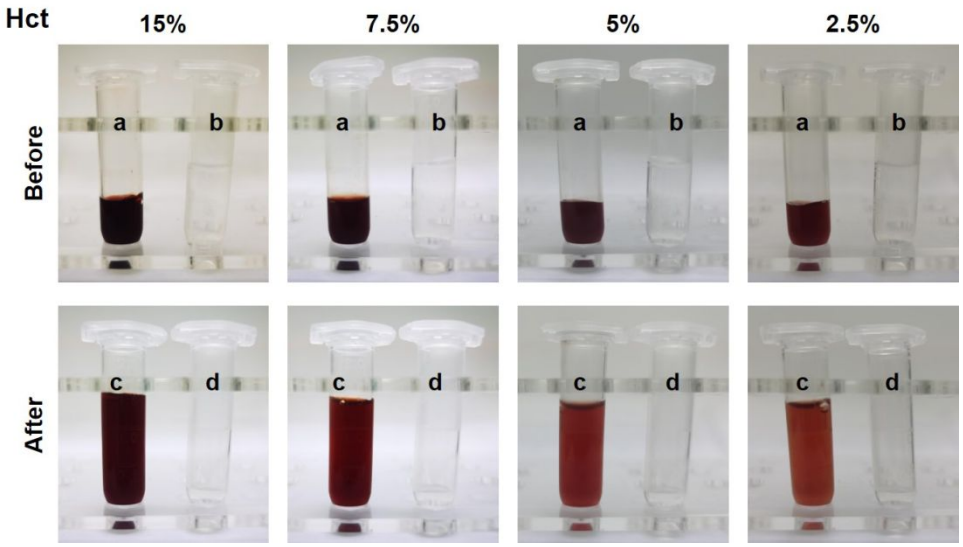

Figure S23. Purification of single cells (100 cells per mL) in different Hct of whole blood sample (Hct: 2.5%, 5%, 7.5%, 15%) by using the optimized microfluidic device at flow rates of 20 µL/min (Inlet 1) and 40 µL/min (Inlet 2). a, b, c, d represent Inlet 1, Inlet 2, Outlet 1, and Outlet 2.

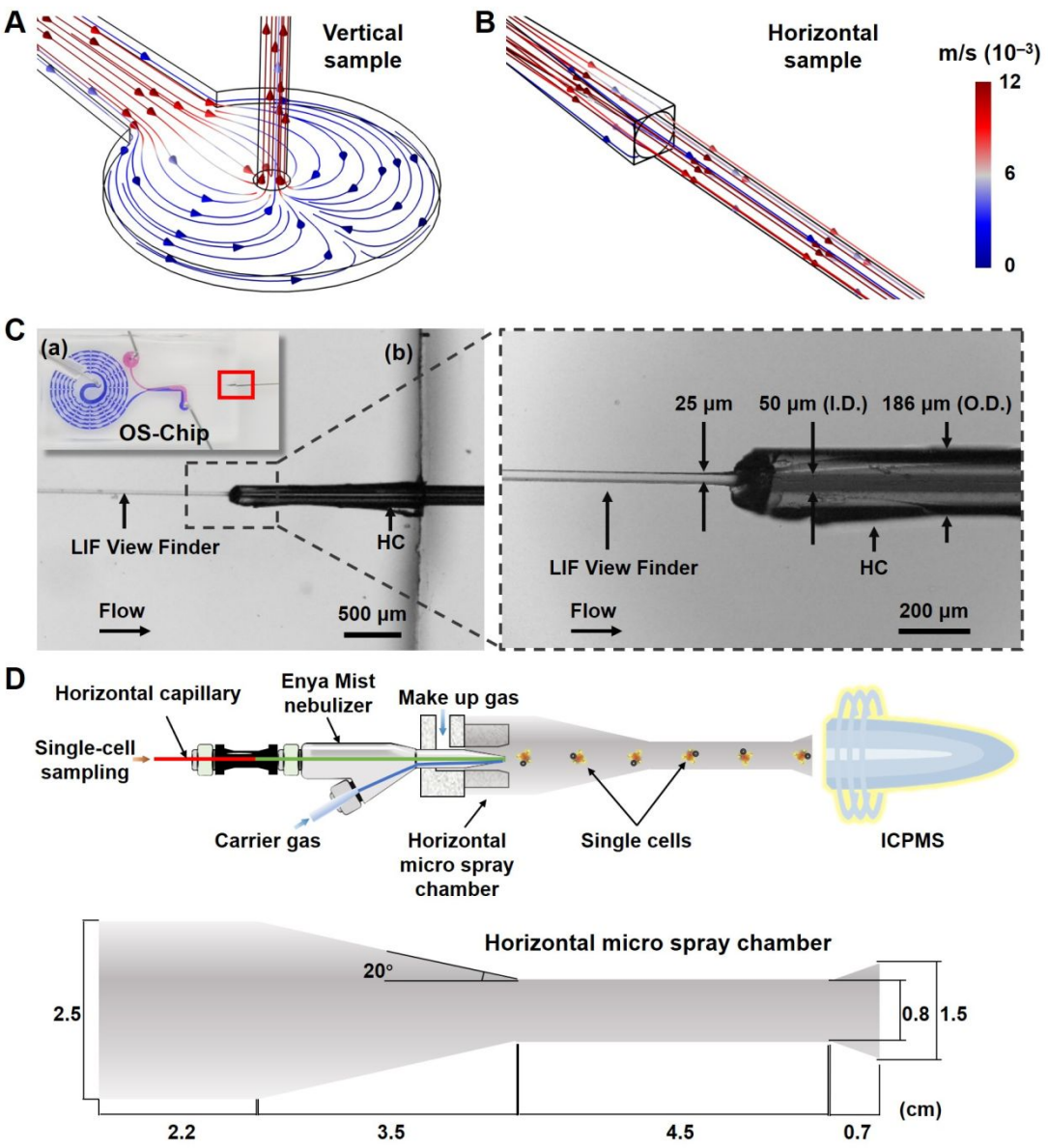

Figure S24. Hydrodynamic simulation of vertical (A) and horizontal (B) sampling models. Inlet 1: 20 μL/mL, Inlet 2: 40 μL/mL. (C) Microscopy image (b) is the close-up of the interface of HC and LIF-VF as highlighted in the red box in photograph of OS-Chip (a). The Enya Mist nebulizer and horizontal micro spray chamber is illustrated in (D).

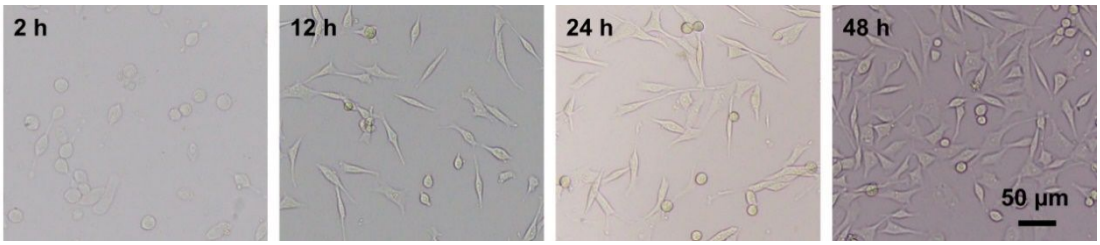

Figure S25. The growth of LoVo cells by reseeding them back into culture for 48 h after collection from the microfluidic chip. Cell viability: 98.91% by MTT assay after 48 h reseeding.

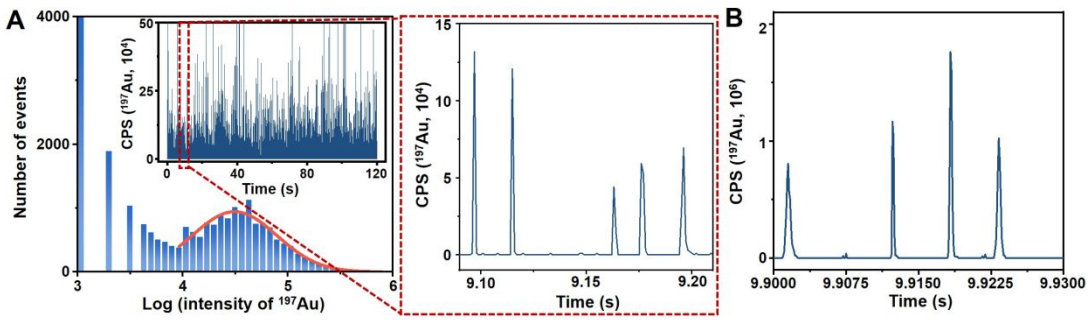

Figure S26. ICP-MS temporal profile and intensity distribution of ^{197}Au spikes in (A) MCF-7 cells by incubating in a medium containing 1.0 μmol L^{-1} Au nanoparticles for the evaluating of measurement efficiency (n = 5, the confidence limit is 95%) and (B) AuNPs solution (10^5 particles/mL^{-1}) introduced from Outlet 2 (conresponding to the enlarged view of Figure 3B).

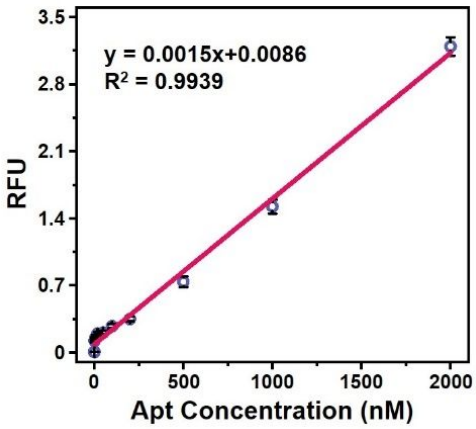

Figure S27. The standard working curves for Sgc8 aptamer (Apt) concentration in LIF. The data indicate mean ± standard deviation (SD). Three independent groups to be tested by using biological replicates (n = 3) were used for each data point.

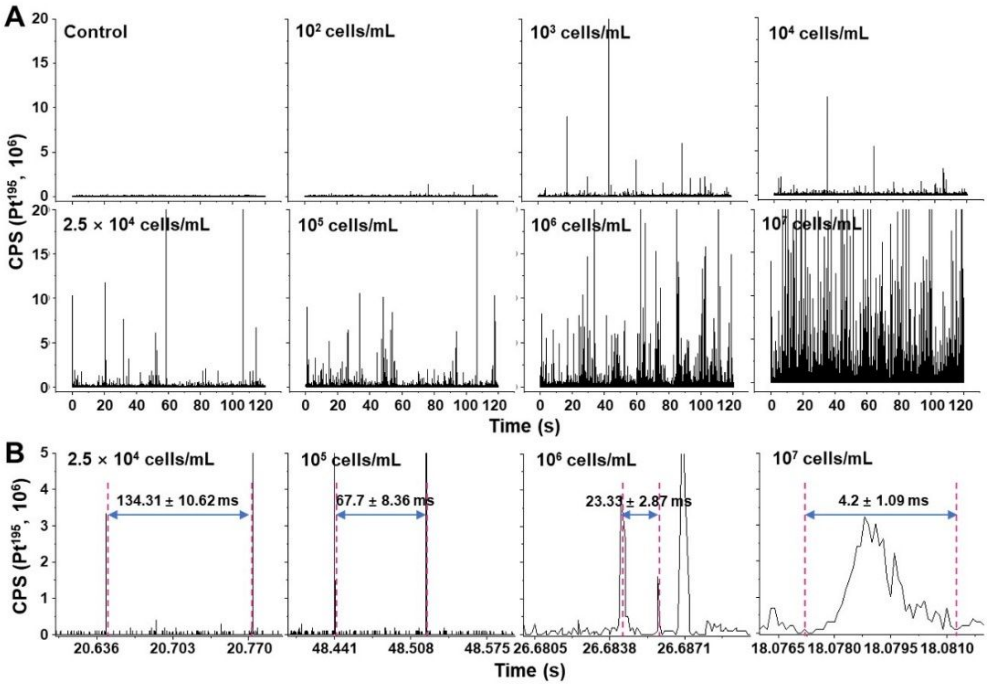

Figure S28. (A) Optimizations of cell number density. MCF-7 cells were used for detection after treatment with 100 μg/L OXA for 6 h. (B) The mean interval between two single-cell events of various cell number density for the MCF-7 cells. The dwell time is set at 0.1 ms (n = 5, the confidence limit is 95%).

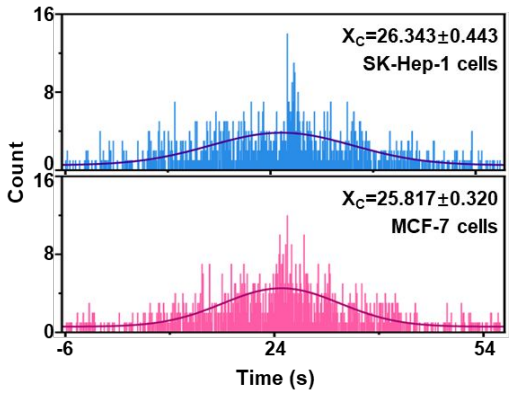

Figure S29. Correction time for two cell lines with detection by LIF-ICP-MS (n = 5, the confidence limit is 95%). LIF-ICP-MS detection was performed on cell suspensions. After screening the LIF-ICP-MS data for single cell signals, the correction time between two by two of the LIF-ICP-MS data was calculated by programming code. Frequency distribution plots and Gaussian fitting were done on the correction time data, and the mean value of X_c (26.080±0.449 s) corresponding to the highest frequency point was recognized as the LIF-ICP-MS uniform correction time.

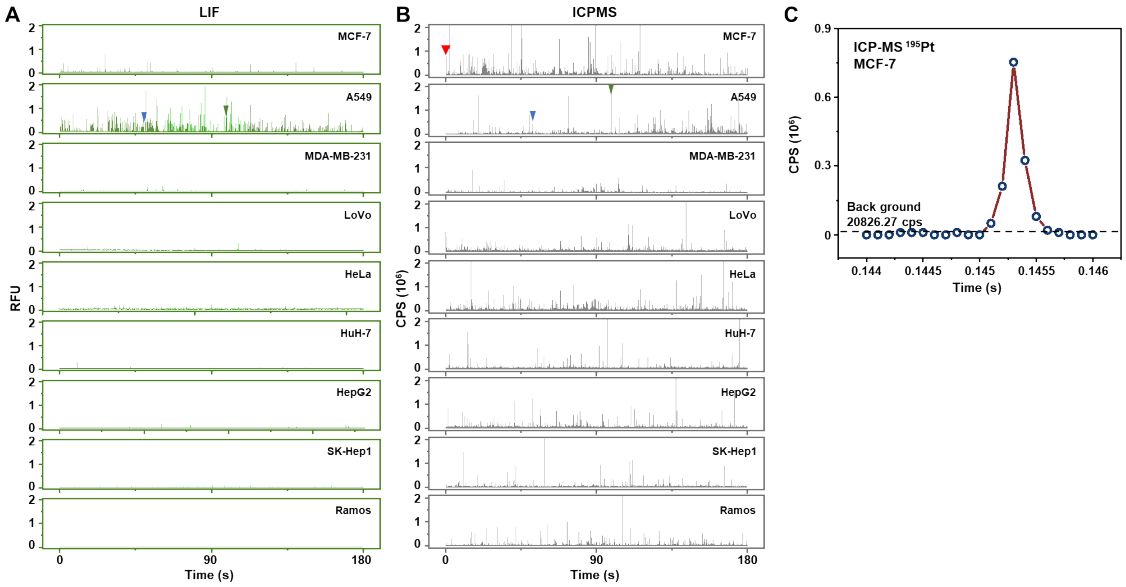

Figure S30. Fluorescence burst data of 6-FAM (A) and ICP-MS temporal profile of ^{195}Pt spikes (B) for various single-cell lines for profiling of PTK7 expression and OXA uptake (n = 5, the confidence limit is 95%). (C) ICP-MS temporal profile of ^{195}Pt in a single MCF-7 cell (corresponding to the red triangles in Figure S30B).

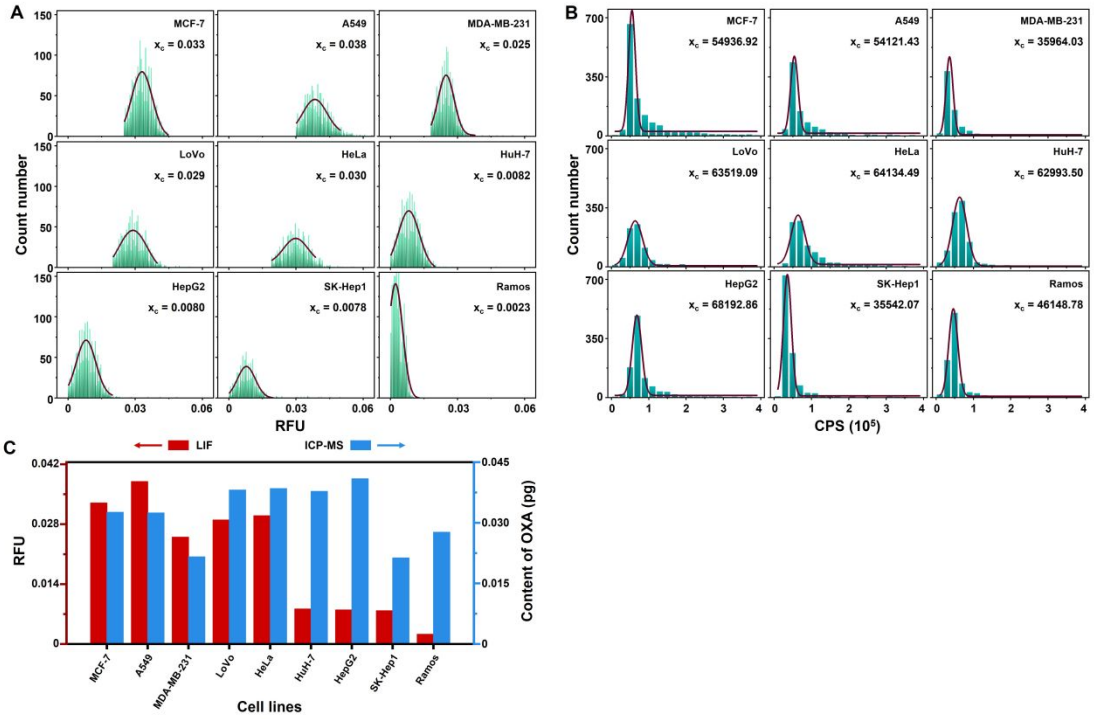

Figure S31. Frequency histogram of peak of single-cell signals and Gauss fit from LIF (A) and ICP-MS (B) (n = 5, the confidence limit is 95%). (C) Histograms of OXA content (signal acquired by ICP-MS) and fluorescence intensity (signal acquired by LIF) in different cell lines.

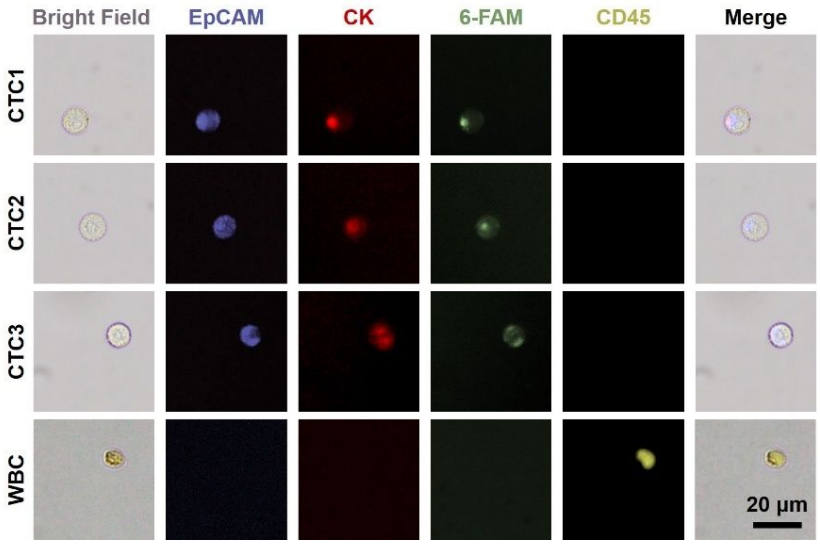

Figure S32. Representative fluorescent images of the CTCs and white blood cell from patient's blood sample. The isolated cells using the microfluidic chip were stained with fluorescent antibodies against epithelial markers (EpCAM), PTK7 (6-FAM) and cytokeratins (CK), and a leukocyte marker (CD45) for leukocyte distinction. CTCs were recognized as $EpCAM^{+}$/ CK^{+}/$6\text{-}FAM^{+}$/$CD45^{-}$ were identified and enumerated as CTCs, while WBCs were recognized as $EpCAM^{-}$/ CK^{-}/$6\text{-}FAM^{-}$/$CD45^{+}$. The fluorescent images of the CTCs and white blood cell were not employed for single-cell analysis.

Table S1. ICP-MS instrumental and operational parameters.

Operating parameter	Setting
ICP forward power (W)	1550
RF frequency (Hz)	27.12
Plasma Ar flow (L/min)	15
Auxiliary Ar flow (L/min)	1
Carrier Ar flow (L/min)	0.99
Makeup Ar flow (L/min)	0.11
Added He flow (mL/min)	5.5
Sampling & intercepting cone material	nickel
Scanning mode	Time-resolved analysis
Dwell time (ms)	0.1
Monitored isotope	^{195}Pt, ^{197}Au

Table S2. Comparation of current status of single-cell analysis to μCytoMS in this work.

Title	Extra sample cleaning	Flow condition	Cell viability	Measurement efficiency	Counting strategy	Throughput/Profiling of an individual cell	Journal
Multi-Dimensional Organic Mass Cytometry: Simultaneous Analysis of Proteins and Metabolites on Single Cells	Centrifugation (2000 rpm, 2 min, 3 times)	1 μL/min	0%	~80%	Flow cytometry	40 cells per min/Proteins & metabolites	Angew. Chem. Int. Ed. (2020)
Proteomic Analysis of Single Mammalian Cells Enabled by Microfluidic Nanodroplet Sample Preparation and Ultrasensitive NanoLC-MS	Centrifugation (3 times)	60 nL/min	Not given	Not given	Microscopic count	21 cells per round/Proteomic analysis	Angew. Chem. Int. Ed. (2018)
Two-Dimensional Cytometry Platform for Single-Particle/Cell Analysis with Laser-Induced Fluorescence and ICP MS	Centrifugation (3 times)	50 μL/min	~93%	29.14%	LIF-ICPMS	2892 cells per min/NA	Anal. Chem. (2021)
Ultrasensitive Ambient Mass Spectrometry Immunoassays: Multiplexed Detection of Proteins in Serum and on Cell Surfaces	Centrifugation (1000 rpm, 4 min, 3 times)	5 μL/min	0%	Not given	MS	20 in total/Protein detection	JACS (2019)
Lanthanide nanoparticles for high sensitivity multiparameter single cell analysis	Centrifugation (220-1500 g, 3 min, 9 times)	Not given	0%	0.5%	Mass cytometry	10000 counts in total/seven biomarkers expression	Chem. Sci. (2019)
Functional Profiling of Circulating Tumor Cells with An Integrated Vortex Capture and Single-Cell Protease Activity Assay	Centrifugation (2300 rpm, 5 min, 3 times)	300 to 2600 μL/min	Living cell	>40%	Hemocytometer	260 cells per min/Protease activity assay	PNAS (2018)
Multiplex profiling of biomarkers and drug uptake in single cells using microfluidic flow cytometry and mass spectrometry	Needless to extra operation	20 μL/min	98.91%	90.60%	LIF-ICP-MS	500 cells per min/Protein & agent uptake	This work

Table S3. Patients' information

Sample No.	Patient Code	Gender	Year	Clinical Investigations	TNM Staging	Therapy	CTC number (/50 μL)
1	526266	Female	42	Breast cancer	NA	Untreated	1.40±0.55 (2, 1, 1, 2, 1)
2	P102	Female	66	Metastatic carcinoma of bone	TxNxM1	Preoperative chemotherapy	2.40±0.55 (3, 3, 2, 2, 2)
3	P072	Female	56	Carcinoma with lymph node metastasis	T2N3M1	Chemotherapy	0.61±0.57 (1, 1, 0, 0, 1)
4	P060	Female	54	Mediastinal lymph node metastasis	T1NxM1	Chemotherapy	3.40±0.50 (3, 3, 3, 4, 4)
5	P162	Female	63	Carcinoma with lymph node metastasis	T2N0M1	Chemotherapy	0.80±0.55 (0, 1, 1, 1, 1)
6	P086	Female	49	Carcinoma with lymph node metastasis	T1NxM1	Chemotherapy	0.40±0.54 (0, 0, 1, 0, 1)
7	P055	Female	56	Breast cancer stage IV	T2N3M1	Chemotherapy	1.00±0.70 (2, 1, 1, 1, 0)
8	P039	Female	48	Nodule in the upper lobe of the right lung	NA	Untreated	1.20±0.83 (1, 2, 2, 0, 1)
9	P091	Female	62	Metastatic carcinoma of bone	TxNxM1	Preoperative chemotherapy	0.60±0.89 (2, 0, 0, 0, 1)
10	P067	Female	46	Breast cancer	NA	Preoperative chemotherapy	0.60±0.55 (1, 1, 1, 0, 0)

References

1. Shen, S. F.; Zhang, F. J.; Wang, S. T.; Wang, J. R.; Long, D. D.; Wang, D. F.; Niu, Y. B., Ultra-low aspect ratio spiral microchannel with ordered micro-bars for flow-rate insensitive blood plasma extraction. Sens. Actuator B-Chem. 2019, 287, 320-328.

2. Wei, X.; Zheng, D.-H.; Cai, Y.; Jiang, R.; Chen, M.-L.; Yang, T.; Xu, Z.-R.; Yu, Y.-L.; Wang, J.-H., High-Throughput/High-Precision Sampling of Single Cells into ICP-MS for Elucidating Cellular Nanoparticles. Anal. Chem. 2018, 90 (24), 14543-14550.

3. Song, Y.; Shi, Y.; Huang, M.; Wang, W.; Wang, Y.; Cheng, J.; Lei, Z.; Zhu, Z.; Yang, C., Bioinspired Engineering of a Multivalent Aptamer-Functionalized Nanointerface to Enhance the Capture and Release of Circulating Tumor Cells. Angew. Chem.-Int. Edit. 2019, 58 (8), 2236-2240.

4. Warkiani, M. E.; Khoo, B. L.; Wu, L.; Tay, A. K. P.; Bhagat, A. A. S.; Han, J.; Lim, C. T., Ultra-fast, label-free isolation of circulating tumor cells from blood using spiral microfluidics. Nat. Protoc. 2016, 11 (1), 134.

5. Rafeie, M.; Zhang, J.; Asadnia, M.; Li, W.; Warkiani, M. E., Multiplexing slanted spiral microchannels for ultra-fast blood plasma separation. Lab Chip 2016, 16 (15), 2791-2802.

6. Shen, S. F.; Tian, C.; Li, T. B.; Xu, J.; Chen, S. W.; Tu, Q.; Yuan, M. S.; Liu, W. M.; Wang, J. Y., Spiral microchannel with ordered micro-obstacles for continuous and highly-efficient particle separation. Lab Chip 2017, 17 (21), 3578-3591.

7. Liu, C.; Xue, C. D.; Sun, J. S.; Hu, G. Q., A generalized formula for inertial lift on a sphere in microchannels. Lab Chip 2016, 16 (5), 884-892.

8. Mitxelena-Iribarren, O.; Zabalo, J.; Arana, S.; Mujika, M., Improved microfluidic platform for simultaneous multiple drug screening towards personalized treatment. Biosens. Bioelectron. 2019, 123, 237-243.

9. Zheng, B.; Tice, J. D.; Roach, L. S.; Ismagilov, R. F., A droplet-based, composite PDMS/glass capillary microfluidic system for evaluating protein crystallization conditions by microbatch and vapor-diffusion methods with on-chip X-ray diffraction. Angew. Chem.-Int. Edit. 2004, 43 (19), 2508-2511.

10. Wu, C.; Wei, X.; Men, X.; Zhang, X.; Yu, Y.-L.; Xu, Z.-R.; Chen, M.-L.; Wang, J.-H., Two-Dimensional Cytometry Platform for Single-Particle/Cell Analysis with Laser-Induced Fluorescence and ICP–MS. Analytical Chemistry 2021, 93 (23), 8203-8209.

11. Lu, Y.; de Vries, W. C.; Overeem, N. J.; Duan, X. X.; Zhang, H. X.; Zhang, H.; Pang, W.; Ravoo, B. J.; Huskens, J., Controlled and Tunable Loading and Release of

Vesicles by Using Gigahertz Acoustics. Angew. Chem.-Int. Edit. 2019, 58 (1), 159-163.

12. Wang, L.; Liu, W. M.; Wang, Y. L.; Wang, J. C.; Tu, Q.; Liu, R.; Wang, J. Y., Construction of oxygen and chemical concentration gradients in a single microfluidic device for studying tumor cell-drug interactions in a dynamic hypoxia microenvironment. Lab Chip 2013, 13 (4), 695-705.

13. Wang, H.; Chen, B. B.; He, M.; Yu, X. X.; Hu, B., Selenocystine against methyl mercury cytotoxicity in HepG2 cells. Sci Rep 2017, 7, 8.

14. Pace, H. E.; Rogers, N. J.; Jarolimek, C.; Coleman, V. A.; Higgins, C. P.; Ranville, J. F., Determining transport efficiency for the purpose of counting and sizing nanoparticles via single particle inductively coupled plasma mass spectrometry. Anal. Chem. 2011, 83 (24), 9361-9369.

15. Wang, H.; Wang, B.; Wang, M.; Zheng, L.; Chen, H.; Chai, Z.; Zhao, Y.; Feng, W., Time-resolved ICP-MS analysis of mineral element contents and distribution patterns in single cells. Analyst 2015, 140 (2), 523-531.

16. Wei, X.; Hu, L. L.; Chen, M. L.; Yang, T.; Wang, J. H., Analysis of the Distribution Pattern of Chromium Species in Single Cells. Anal. Chem. 2016, 88 (24), 12437-12444.

17. Zhang, X.; Wei, X.; Men, X.; Jiang, Z.; Ye, W.-Q.; Chen, M.-L.; Yang, T.; Xu, Z.-R.; Wang, J.-H., Inertial-Force-Assisted, High-Throughput, Droplet-Free, Single-Cell Sampling Coupled with ICP-MS for Real-Time Cell Analysis. Anal. Chem. 2020, 92 (9), 6604-6612.

18. Gou, Y.; Zhang, S.; Sun, C.; Wang, P.; You, Z.; Yalikun, Y.; Tanaka, Y.; Ren, D., Sheathless Inertial Focusing Chip Combining a Spiral Channel with Periodic Expansion Structures for Efficient and Stable Particle Sorting. Analytical Chemistry 2020, 92 (2), 1833-1841.

19. Mu, T.; Toyoda, H.; Kimura, Y.; Yamada, M.; Utoh, R.; Umeno, D.; Seki, M., Laborless, Automated Microfluidic Tandem Cell Processor for Visualizing Intracellular Molecules of Mammalian Cells. Analytical Chemistry 2020, 92 (3), 2580-2588.

20. Zhang, X.; Wei, X.; Men, X.; Wu, C.-X.; Bai, J.-J.; Li, W.-T.; Yang, T.; Chen, M.-L.; Wang, J.-H., Dual-Multivalent-Aptamer-Conjugated Nanoprobes for Superefficient Discerning of Single Circulating Tumor Cells in a Microfluidic Chip with Inductively Coupled Plasma Mass Spectrometry Detection. ACS Applied Materials & Interfaces 2021, 13 (36), 43668-43675.

21. Wang, J.; Wei, X.; Wu, C.-X.; Zhang, X.; Wei Y.-J.; Liu J.-H.; Wang Y.; Chen, M.-L.; Wang, J.-H., Interaction of Cellular Uptake of Nanosilver and Metallothionein Stress Expression Elucidated by 2D Single-Cell Analyses Based on LIF and ICP-MS. Analytical Chemistry 2020, 95 (44), 16176-16184.